IEEE Journal of Microwaves

Received 31 August 2023; revised 16 October 2023 and 15 November 2023; accepted 16 November 2023. Date of publication 11 December 2023; date of current version 8 January 2024.

Digital Object Identifier 10.1109/JMW.2023.3334757

Signal Model for Coherent Processing of Uncoupled and Low Frequency Coupled MIMO Radar Networks

VINZENZ JANOUDI [1] (Graduate Student Member, IEEE), PIRMIN SCHOEDER [1] (Member, IEEE), TIMO GREBNER [1] (Graduate Student Member, IEEE), NILS APPENRODT [2] (Senior Member, IEEE), JUERGEN DICKMANN [2] (Senior Member, IEEE), AND CHRISTIAN WALDSCHMIDT [1] (Fellow, IEEE)

(Regular Paper)

[1]Institute of Microwave Engineering, Ulm University, 89077 Ulm, Germany
[2]Radar and Perception, Mercedes-Benz Group AG, 71063 Sindelfingen, Germany

CORRESPONDING AUTHOR: Vinzenz Janoudi (e-mail: vinzenz.janoudi@uni-ulm.de).

ABSTRACT MIMO radar networks consisting of multiple independent radar sensors offer the possibility to create large virtual apertures and therefore provide high angular resolution for automotive radar systems. In order to increase the angular resolution, the network must be able to process all data phase coherently. Establishing phase coherency, without distributing the transmitted RF signal to all sensors, poses a significant challenge in the automotive frequency range of 76 GHz to 81 GHz. This paper presents a signal model for uncoupled and low frequency coupled radar networks. The requirements for phase coherent processing for uncoupled radar sensors are systematically derived from the signal model. The proposed signal processing methods, which establish coherency, are sub-aperture based. Both the signal model and the proposed signal processing methods are verified by measurements with radar sensor networks composed of 2 and 3 radar sensors, providing 768 and 1728 virtual channels respectively. Measurements verify that phase noise is insignificant in the process of establishing coherency in uncoupled and low frequency coupled radar networks.

INDEX TERMS Automotive radar networks, signal processing, multiple-input-multiple-output.

I. INTRODUCTION

Driver assistance systems' demands towards the imaging capabilities of radar systems are ever increasing. In light of these demands, higher Direction of Arrival (DoA) resolution is required [1]. As the requirements rise, it becomes increasingly challenging to address these demands with a single sensor radar system [2]. Multiple-Input-Multiple-Output (MIMO) radar networks, consisting of multiple individual MIMO sensors, offer the possibility to place the sensors further apart and thereby increase the aperture of the virtual antenna array. Multiple of MIMO radar networks have already been realized and analyzed [3], [4], [5], [6], [7], [8]. The different implementations are divided into three network topologies: Radio Frequency (RF) coupled networks, Low Frequency (LF) coupled networks and uncoupled networks. The three topologies are depicted in Fig. 1.

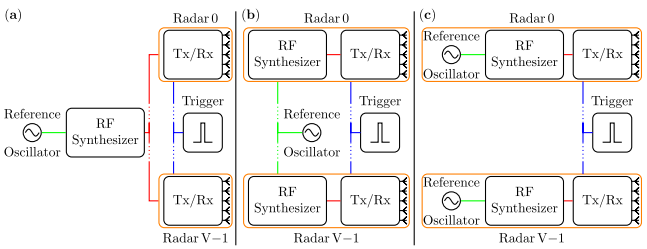

FIGURE 1. Different hardware topologies for MIMO radar networks. (a) RF coupled network. (b) LF coupled network. (c) uncoupled network.

The simplest realization is the RF coupled topology, whose unique feature is the distribution of the RF signal to each radar sensor. RF coupled networks preserve the coherency of Phase Noise (PN) and therefore benefit from the range-correlation effect [9].

In [10], a Chirp-Sequence Frequency Modulated Continuous Wave (CS-FMCW) radar network according to Fig. 1(a) is presented, which distributes the RF signal with semi-rigid cables at a fourth of the transmit signal frequency. Due to the CS-FMCW modulation scheme, each sensor simply uses a frequency multiplier to create the required 77 GHz signal. The network consists of 2 sensors with a total of 768 Virtual (Vx) channels. This approach eases the requirements on the signal distribution, but semi-rigid cables at 20 GHz still significantly attenuate the signal and are sensitive to phase variations under mechanical stress.

The LF coupled network topology, Fig. 1(b), distributes an LF clock derived from a single reference oscillator instead of the RF signal. From the reference clock, the multiple times higher RF signal is synthesized. This still requires a signal distribution, but since the distributed signal has a significantly lower frequency than the actual transmit signal, complexity and costs are drastically lower than for the RF coupled topology.

In [5], a network with CS-FMCW modulation and Frequency Division Multiplexing (FDM) is presented, in which the reference frequency is 80 MHz, while the synthesized transmit signal frequency is 77 GHz. The network realizes 32 Vx channels with 2 radar sensors.

A different realization was shown in [7], in which a CS-FMCW modulation-based network and Time Domain Multiplexing (TDM) was used. The distributed reference frequency is 100 MHz, while the synthesized transmit signal frequency is 154 GHz. The network realizes 64 Vx channels with 2 radar sensors.

The most flexible, but also most challenging, network topology is the uncoupled network topology, in which each radar sensor synthesizes the RF signal from independent reference oscillators, Fig. 1(c).

In [6] and [11], uncoupled radar networks with CS-FMCW and FDM are presented, operating at 122 GHz, derived from uncoupled 100 MHz oscillators. The networks are able to coherently detect the range [6] and velocity [11] of a target with a total of 6 Vx channels with 3 radar sensors.

In [7] and [8], radar networks operating at 154 GHz, synthesized from reference frequencies of 100 MHz and 10 GHz respectively, are presented. Both networks realize 64 Vx channels with 2 radar sensors. These networks require a calibration target with known position to establish coherency.

The topologies investigated in this work are LF coupled and uncoupled networks; the individual sensors are triggered by an independent central trigger source. In contrast to previous works, the presented signal model incorporates the fact that not only the RF signal is derived from the reference oscillator but also all intra frame and intra chirp timings.

A signal model including the coupling-induced errors is derived, which is used to calculate boundaries in terms of frequency deviation for the reference oscillators. The boundaries heavily depend on the transmit frequency, the reference oscillator's frequency, and the radar waveform parameters. Signal processing methods are presented to estimate and correct the coupling-induced errors on the radar signals to achieve fully coherent processing of the complete network in the range, velocity, and angular domain. None of the presented estimation and correction methods require targets with known positions or require the presence of single scatter targets.

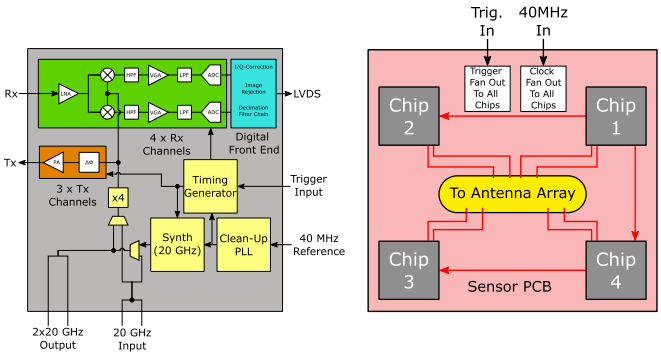

FIGURE 2. Left: block diagram of a single radar chip. Right: block diagram of a single radar sensor.

To verify the signal model and the derived boundaries, networks consisting of 2 and 3 radar sensors with 768 and 1728 Vx channels, respectively, are used. The reference clocks are provided by Temperature-Compensated Voltage-Controlled Crystal Oscillator (TCVCXO) and the radar sensors are realized by multiple state-of-the-art automotive graded MIMO radar chips.

The structure of the paper is as follows: Section II describes the structure of the individual parts of the radar network. In Section III, the influence of the reference oscillator's frequency deviation on the timing generation and the RF signal is described. Section IV introduces the used notation and investigates the spectrum of a chirp. The signal model and boundaries for the frequency deviation of the reference clocks are discussed in Section V. In Section VI, the necessary estimation and correction methods to coherently process the complete network are presented. Finally, in Section VII measurements for different radar network topologies and varying sizes in an anechoic chamber are presented and compared to the theoretical signal model. The section ends with outdoor measurements of a moving extended target using the uncoupled 2-sensor radar network.

II. SYSTEM DESCRIPTION

First, the realized radar network is described to better understand the presented signal model. The derived signal model is universally applicable to all radar networks in which the single sensors derive the timings and the RF signal from a common reference oscillator. The realized network consists of multiple individual MIMO sensors, which in turn consist of multiple state-of-the-art MIMO radar chips, specified for automotive applications.

A. CHIP DESCRIPTION

A single radar chip provides 3 Transmit (Tx) and 4 Receive (Rx) channels. The block diagram of a single chip is depicted on the left in Fig. 2. The chip requires only a single reference

frequency, $f_c = 40$ MHz to operate. From this reference frequency, all timings, clocks, and the RF signals are derived.

The first stage for the reference clock is a clean-up Phase-Locked Loop (PLL) having a narrow loop bandwidth for removing noise and interferences picked up by the reference clock signal [12]. The consequence of this narrow loop bandwidth is that the PN of the clock driving the synthesizer and timing generator is predominantly determined by the internal PN of the PLL itself and the Voltage Controlled Oscillator (VCO) [12]. Therefore, the PN of the reference oscillator is insignificant.

The timing generator creates the intra chirp and the intra frame timings, while the RF synthesizer creates the chirps, which are transmitted and used for downmixing.

B. SENSOR DESCRIPTION

A single sensor is composed of 4 radar chips, which are jointly triggered and provided with the same reference clock. The reference clock on the sensor is distributed to all chips via a 1-to-4 clock buffer. Every chip independently derives the intra frame and intra chirp timings from the reference clock. The block diagram of a single sensor is depicted on the right in Fig. 2.

The 4 MIMO radar chips provide each sensor with 12 Tx channels per sensor P_S and with 16 Rx channels per sensor Q_S. The chips are divided into a primary chip, namely chip 1, and secondary chips, chip 2, 3, and 4. Chip 1 uses its RF synthesizer to create the chirps, the RF synthesizers of the secondary chips are disabled. The chirps of chip 1 are distributed to the secondary chips, which they transmit and feed the mixers of the receive channels. The daisy chain chirp distribution scheme introduces additional time delays, which add up to the time-of-flight τ. The additional time delays are ignored, since they are time invariant and are estimated and corrected during the calibration process.

For the uncoupled network topology, all sensors of the network are provided with reference clocks from independent oscillators. In contrast, in the LF network topology, all sensors of the network are provided with the clock from a single reference oscillator.

C. VIRTUAL NETWORK ANTENNA APERTURE AND SUB-APERTURES

A network is composed of V sensors, in which each sensor is equipped with an individual antenna array containing P_S Tx and Q_S Rx antenna elements.

Due to the coherent processing of the network, all antenna elements form a joint virtual network aperture. Throughout the derivation of the signal model, it is necessary to divide the complete virtual aperture into multiple sub-apertures, since a joint DoA estimation is only possible after multiple correction steps on all channels included in a sub-aperture.

The joint network virtual aperture is split in mono- and bistatic sub-apertures. In this context, the terms mono- and bistatic apply to the sensor level.

TABLE 1. 2-Sensor Network Aperture Properties

Parameter	Value
Horizontal Element Spacing Δx	8 mm
Vertical Element Spacing Δz	5 mm
Horizontal Network Aperture Size X_{Network}	0.48 m
Horizontal Sub-Aperture Size $X_{m,n}$	0.12 m
Vertical Aperture Size $Z = Z_{m,n}$	0.055 m
Number of Vx Elements of $\lvert\Lambda\rvert$	768
Number of Vx Elements of $\lvert\Lambda_{m,n}\rvert$	192
Azimuth Resolution of a Sub-Aperture $\delta\theta_{m,n}$	1.6°
Azimuth Resolution of the Network Aperture $\delta\theta$	0.42°
Elevation Resolution $\delta\phi_{m,n} = \delta\phi$	3.3°

The position of a virtual element is described by

$$\mathbf{x}_{\text{Vx},m,n,q,p} = \mathbf{x}_{\text{Rx},m,q} + \mathbf{x}_{\text{Tx},n,p}, \tag{1}$$

where $\mathbf{x}_{\text{Vx},m,n,q,p}$ describes the virtual antenna position created when the p-th, $p \in [0 \ldots P_S - 1]$, Tx antenna located on the m-th, $m \in [0 \ldots V - 1]$, sensor transmits and the q-th, $q \in [0 \ldots Q_S - 1]$, Rx antenna located on the n-th, $n \in [0 \ldots V - 1]$, sensor receives.

A sub-aperture is described by the set of positions generated by all Q_S Rx antennas of the m-th sensor and all P_S Tx antennas of the n-th sensor and is denoted as $\Lambda_{n,m}$. Λ, in turn, describes the set of all positions in the network. The number of sub-apertures in a network consisting of V sensors is V^2. From the V^2 sub-apertures, V sub-apertures are monostatic, $m = n$, and $V^2 - V$ bistatic, $m \neq n$.

A bistatic pair is formed by 2 sets of Vx antennas generated by 2 sensors. One set of the pair is formed by the m-th sensor's Tx antennas and the n-th sensor's Rx antennas, $\Lambda_{m,n}$. The other half of the pair is generated by the n-th sensor's Tx antennas and the m-th sensor's Rx antennas, $\Lambda_{n,m}$.

Redundant Vx antenna elements play a crucial role in the process of establishing coherency between sub-apertures and are created if multiple unique pairs of Rx and Tx antenna positions exist which result in the same Vx position vector. In Fig. 3, the virtual network aperture for the 2-sensor network and its sub-apertures is depicted.

The complete virtual network aperture of the 2-sensor radar network consists of 4 sub-apertures, 2 monostatic apertures and 2 bistatic apertures. The 2 bistatic sub-apertures form a bistatic pair. The virtual aperture of the 2-sensor network contains redundant elements on each transition from sub-aperture to sub-aperture. The properties of the virtual antenna aperture and its sub-apertures are listed in Table 1.A detailed description of the antenna array can be found in [10].

The large size of the network aperture leads to a violation of the far-field condition in the measurement range of the radar network [13], [14]. The focus of this paper is on the network coupling effects. As the problem of far-field condition violation is independent from the coupling mechanism of the network, it is neglected throughout the derivation of the signal model.

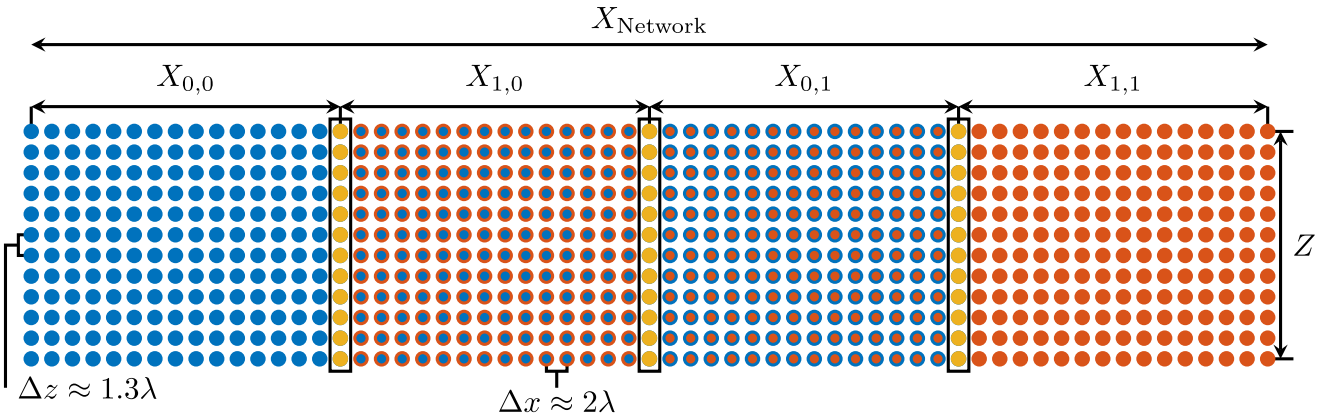

FIGURE 3. Virtual aperture and sub-apertures of the 2-sensor radar network. The color of the ring indicates the sensor affiliation of the Tx antenna, the color of the circle indicates the sensor affiliation of the Rx antenna. Yellow elements are redundant Vx antenna elements.

III. OSCILLATORS & TIMINGS

In the actual case of an uncoupled topology, each sensor is provided with its own independent clock with frequency $f_{c,n}$. For the signal model, the absolute frequencies of the oscillators are less important, whereas the pairwise relative frequency deviation from oscillator to oscillator is significant. Therefore, one of the two oscillators of a pair is arbitrarily defined as the oscillator with the nominal frequency $f_c = f_{c,m}$, and the other is defined with a frequency deviation:

$$f_{c,n} = f_{c,m} + (f_{c,n} - f_{c,m}) = f_{c,m} + \Delta f_{n,m}. \tag{2}$$

For the LF coupled topology, all sensors are provided with the same clock derived from a single oscillator with frequency $f_{c,0}$. The frequency difference, therefore, is always $\Delta f = 0$ Hz.

The used oscillators are TCVCXO, which are frequency tunable by a potentiometer and equipped with a clock buffer providing multiple phase coherent rectangular shaped outputs. The signal model assumes that the frequencies of the individual oscillators are fixed for the duration of a frame but can change from frame to frame. In the following, the random variable behavior of the frequency is dropped, but the frequency deviation must always be lower than the derived limits.

In Fig. 4, the RF signal and the timings created by the synthesizer and the timing generator are depicted. At the point in time t_0 the chip receives an external frame trigger signal, the remaining intra chirp and intra frame timings required are created by the timing generator and therefore only dependent on the reference clock. The RF synthesizer is triggered by the timing generator to generate chirps with slope S for the duration T_{Up}. The slope is expressed in terms of starting frequency f_0, end frequency f_1 and ramp up time, T_{Up} as

$$S = \frac{f_1 - f_0}{T_{\text{Up}}} = \frac{BW}{T_{\text{Up}}}. \tag{3}$$

The Analog-To-Digital Converter (ADC) starts to sample the received Intermediate Frequency (IF) signal after the time

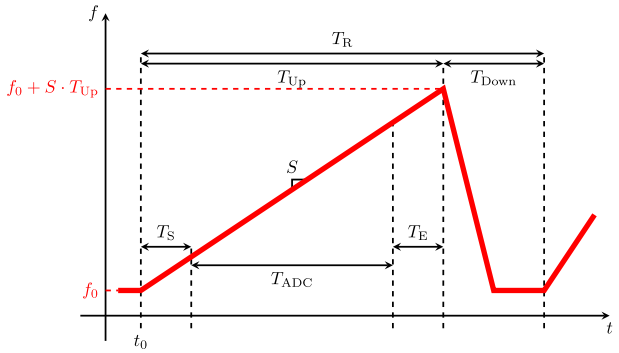

FIGURE 4. Chirp signal and timings created by the synthesizer and the timing generator.

duration T_{S}, which is defined relative to the start of a chirp. The time T_{S} is largely determined by the settling effects of the High Pass Filter (HPF) and the time-of-flight τ. The ADC receives the start trigger from the timing generator and samples N_{s} samples at the frequency f_{s}, which determines the sampling time $T_{\text{ADC}} = \frac{N_{\text{s}}}{f_{\text{s}}}$. Well-designed waveforms choose a ramp time which is longer than the sum of T_{s} and T_{ADC}, due to the group delay of the digital filter chain. At the end of the chirp, the timing generator triggers the RF synthesizer to ramp its VCO down. T_{Down} is determined by the chirp bandwidth; the larger the chirp bandwidth, the longer T_{Down} must be chosen for a clean signal. The chirp repetition period T_{R} is the sum of T_{Up} and T_{Down} and determines when the next chirp starts.

A. TIMINGS

Timings are created by counting clock cycles, a counter must count $N_{\text{CLK}} = \widetilde{T} f_{\text{c}}$ number of cycles in order to create a timing signal of time duration $\widetilde{T}$. The number of cycles are calculated based on the nominal frequency at which the counter is driven. Since the counters of the radar sensors are driven by oscillators with different frequencies, this leads to

different time durations for the same counter value. The time duration $\widetilde{T}_m$ therefore becomes sensor specific, but since oscillators are always treated pairwise, one of the two oscillators is chosen as the nominal one, $\widetilde{T} = \widetilde{T}_m$. This is written as

$$\widetilde{T}_m = N_{\mathrm{CLK}} \cdot T_{\mathrm{c},m} = N_{\mathrm{CLK}} \cdot \frac{f_{\mathrm{c}}}{f_{\mathrm{c},m}} = \widetilde{T} \cdot \frac{f_{\mathrm{c}}}{f_{\mathrm{c}}}, \tag{4}$$

where the last part follows from the fact that the m-th oscillator was chosen to be the nominal one. The partner oscillator counts the same number of cycles and creates a different time duration:

$$\widetilde{T}_n = N_{\mathrm{CLK}} \cdot T_{\mathrm{c},n} = \widetilde{T} \cdot \frac{f_{\mathrm{c}}}{f_{\mathrm{c}} + \Delta f_{n,m}}. \tag{5}$$

The time difference from the point of view of oscillator $f_{\mathrm{c},m}$, occurring while both oscillators count the same number of cycles, N_{CLK}, is then

$$\Delta\widetilde{T}_{m,n} = \widetilde{T}_m - \widetilde{T}_n = \widetilde{T} \cdot \left(1 - \frac{1}{1 + \frac{\Delta f_{n,m}}{f_{\mathrm{c}}}}\right). \tag{6}$$

From the perspective of oscillator $f_{\mathrm{c},n}$, the timing difference is the same but with opposing sign:

$$\Delta\widetilde{T}_{n,m} = \widetilde{T}_n - \widetilde{T}_m = -\Delta\widetilde{T}_{m,n} = \widetilde{T} \cdot \left(\frac{1}{1 + \frac{\Delta f_{n,m}}{f_{\mathrm{c}}}} - 1\right). \tag{7}$$

If the frequency $f_{\mathrm{c},n}$ is higher than $f_{\mathrm{c},m}$, $\Delta f_{n,m} \geq 0$, the timings of $f_{\mathrm{c},m}$ are always too late, whereas from the perspective of oscillator $f_{\mathrm{c},m}$, the timings of $f_{\mathrm{c},n}$ are too early.

It is important to note that the relative time difference $\Delta\widetilde{T}$ with $\widetilde{T}$. For the radar use case, this means that with the progression of the frame, the timing difference between the sensors increases: Because at the beginning of the frame only a frame trigger is issued and the intra frame timings are created by the sensor specific timing generators in reference to the frame trigger. The time duration is always with respect to the current frame trigger.

For LF coupled networks, the timing errors are always 0, since the frequency deviation is 0, $f_{\mathrm{c},m} = f_{\mathrm{c},n} = f_{\mathrm{c}}$.

B. FREQUENCY SYNTHESIS

The RF chirp signal is created by a synthesizer, which is a time variant frequency multiplier. From the perspective of the oscillator $f_{\mathrm{c},m}$ the start frequency of the chirp f_0, is created by multiplying the reference frequency by the factor N_0:

$$f_{0,m} = N_0 \cdot f_{\mathrm{c},m}. \tag{8}$$

The final chirp frequency is achieved with the final frequency multiplication factor $N_1 = N_0 + \Delta N$

$$f_{1,m} = N_1 \cdot f_{\mathrm{c},m} = (N_0 + \Delta N) \cdot f_{\mathrm{c},m}. \tag{9}$$

The frequency of oscillator $f_{\mathrm{c},n}$ is multiplied by the same factors N_0 and N_1, which leads to a relative frequency deviation between the radar sensors.

The RF signals created by the synthesizer driven by $f_{\mathrm{c},n}$ is expressed in terms of $f_{\mathrm{c},m}$ and $\Delta f_{n,m}$. This is used to get the frequency difference of the RF start frequency, $\Delta f_{0,m,n}$, end frequency $\Delta f_{1,m,n}$, and bandwidth $\Delta BW_{n,m}$ in relation to the reference frequencies.

As for the timing, the point of view is crucial. From the point of view of the oscillator which runs at the lower frequency, the other oscillator starts and stops at frequencies which are too high. This is reversed from the perspective of the oscillator with the higher frequency; the other clock starts and stops at too low a frequency. The frequency and slope deviations are of the same magnitude but with reversed signs, depending of the point of view.

IV. SIGNAL THEORY

This section's aim is the introduction and derivation of mathematical expressions which are repeatedly employed during the derivation of the signal model.

A. MATHEMATICAL NOTATION

The fundamental function of modern CS-FMCW radar systems is the time limited sampled sinusoidal function which is described as

$$x(n) = \begin{cases} |A| \mathrm{e}^{\mathrm{j}\varphi_0} \mathrm{e}^{\mathrm{j}2\pi \frac{f_0}{f_{\mathrm{s}}} n} & 0 \leq n \leq N-1 \\ 0 & \text{else} \end{cases}, \tag{10}$$

in which $|A|$ is the magnitude, φ_0 the starting phase, which together form the complex amplitude $A = |A|\mathrm{e}^{\mathrm{j}\varphi_0}$, f_0 the frequency of the signal, $f_{\mathrm{s}} = \frac{1}{T_{\mathrm{s}}}$ the sampling rate in Hertz, and N the observation interval in number of samples. The signal model and the estimation and correction of the coupling-induced errors are described in the frequency domain. The spectrum of (10), [15] is

$$\begin{aligned} X(f) &= \sum_{n=0}^{N-1} A \cdot \mathrm{e}^{\mathrm{j}2\pi \frac{f_0}{f_{\mathrm{s}}} n} \mathrm{e}^{-\mathrm{j}2\pi \frac{f}{f_{\mathrm{s}}} n} \\ &= A \cdot \mathrm{e}^{-\mathrm{j}2\pi \frac{f-f_0}{f_{\mathrm{s}}} \frac{N-1}{2}} N T_{\mathrm{s}} \frac{\sin\left(\pi \frac{f-f_0}{f_{\mathrm{s}}} N\right)}{\sin\left(\pi \frac{f-f_0}{f_{\mathrm{s}}}\right) N T_{\mathrm{s}}}. \end{aligned} \tag{11}$$

The frequency resolution δf is defined as the frequency difference between the maximum of (11) and its first zero, which is given by

$$\delta f = \frac{f_{\mathrm{s}}}{N} = \frac{1}{T_{\mathrm{s}} \cdot N}. \tag{12}$$

The Fast Fourier Transform (FFT) is used to compute the spectra of equidistant sampled data and is the frequency discrete and scaled version of the Time Discrete Fourier Transform (TDFT) [15]. This means that in situations in which no analytical spectrum is available, the FFT can be used to evaluate the TDFT at discrete frequencies. Measurement data are always processed by the FFT and additional windowing [16]. Throughout this paper, the signal of the radar is derived time continuously, and the time discretization is implicit. This means that the spectra of the signals are described by the TDFT. The windowing of the signal is omitted for the

sake of easier notation and the following shorthand notation for the spectrum is used,

$$H_N(f-f_0) = \mathrm{e}^{\mathrm{j}2\pi\frac{f-f_0}{f_\mathrm{s}}\frac{N-1}{2}} NT_\mathrm{s} \frac{\sin\left(\pi\frac{f-f_0}{f_\mathrm{s}}N\right)}{\sin\left(\pi\frac{f-f_0}{f_\mathrm{s}}\right)NT_\mathrm{s}} * X_\mathrm{Window}(f), \quad (13)$$

where the $(*)$ operator indicates convolution, and $X_\mathrm{Window}(f)$ is the Time Continuous Fourier Transform (TCFT) of the window. Including windowing, this allows (11) to be written more clearly as

$$X(f) = AH_N(f-f_0). \quad (14)$$

For the sake of simplicity, the explicit dependency on the sampling rate is dropped, since the context will make it self explanatory which sampling frequency must be used. The TDFT describes the spectra in all radar dimensions. In order to distinguish between the dimensions, the frequency variables f of the spectra are denoted with a subscript indicating the dimension. The range is associated with the fast time frequency. The frequency variable is denoted as f_R and the frequency resolution as δf_R. The velocity is associated with the slow time frequency. The frequency variable is denoted as f_v and the frequency resolution as δf_v.

B. SPECTRUM OF A CHIRP

During the investigation regarding the coupling influence on the CS-FMCW signal structure, a time limited sinusoidal oscillation with a residual chirp bandwidth occurs. This is mathematically described in continuous time as

$$x(t) = \begin{cases} A\cdot\mathrm{e}^{\mathrm{j}2\pi f_0 t}\mathrm{e}^{\mathrm{j}\pi S t^2} & 0 \le t \le T \\ 0 & \text{else} \end{cases}, \quad (15)$$

in which S describes the chirp rate in Hz s^{-1}. The corresponding time discrete version is described by

$$x(n) = \begin{cases} A\cdot\mathrm{e}^{\mathrm{j}2\pi\frac{f_0}{f_\mathrm{s}}n}\mathrm{e}^{j\pi\frac{S}{f_\mathrm{s}^2}n^2} & 0 \le n \le N-1 \\ 0 & \text{else} \end{cases}. \quad (16)$$

For a more general and easier investigation of (16), the chirp rate is defined as the ratio of the bandwidth B covered by the chirp over the course of the observation interval $T = N\cdot T_\mathrm{s}$. Furthermore, the bandwidth B is expressed in multiples of the frequency resolution, δf, which results in

$$S = \frac{B}{T} = \frac{\alpha\cdot\delta f}{N\cdot T_\mathrm{s}} = \alpha\frac{f_\mathrm{s}^2}{N^2}, \quad (17)$$

in which the parameter α describes the amount of bandwidth covered by the chirp in terms of bins over the course of time duration T. Due to the lack of a closed form expression for the spectrum of (16), a numerical investigation via the FFT is carried out. In Fig. 5 the FFT-based calculated power spectra of (16) for values of α greater than a frequency bin is shown. From Fig. 5 it is deduced that for a chirp with a bandwidth larger than a frequency bin width, the spectrum is significantly spread over multiple frequency bins, which leads to a loss of frequency resolution.

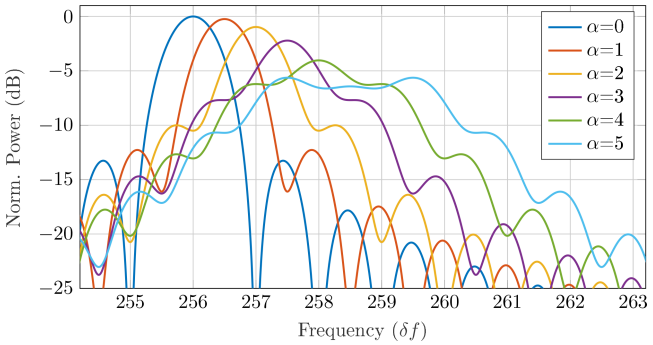

FIGURE 5. FFT-based evaluation of the power spectrum for the signal defined by (16) for varying α and fixed parameter of $N = 1024$, $f_\mathrm{s} = 10$ MHz, $f_0 = 2.5$ MHz, and $A = 1$.

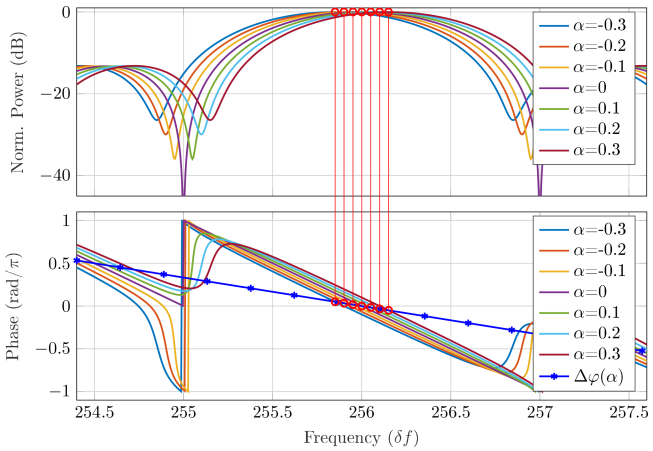

FIGURE 6. FFT-based evaluation of the spectrum for the signal defined by (16) for varying α and fixed parameter of $N = 1024$, $f_\mathrm{s} = 10$ MHz, $f_0 = 2.5$ MHz, and $A = 1$.

In Fig. 6 the FFT-based spectra (16) for chirps with significantly smaller chirp bandwidth than a frequency bin width are shown. The red circles highlight the frequencies, f_max, at which the power spectra of the signals have a maximum. It can be seen that the dominant influence of the chirp bandwidth α is a frequency shift of the maximum in the frequency domain. A quantitative evaluation of the additional frequency shift of the maximum in the frequency domain shows that a residual chirp with the covered bandwidth α introduces an additional frequency shift of $\alpha\frac{\delta f}{2}$. The loss of resolution is negligible. The frequency maximum of the spectrum of (16) is therefore described by

$$f_\mathrm{max} = \arg\max\left(|X(f)|^2\right) \approx f_0 + \alpha\frac{\delta f}{2} = f_0 + \alpha\Delta f, \quad (18)$$

where the factor $\frac{\delta f}{2}$ is condensed to Δf for clearer notation. The loss of power in the spectrum, evaluated at the maximum depending on the chirp bandwidth, is less than 0.2 dB and therefore neglectable for $|\alpha|<0.1$.

For a pure sinusoidal signal, $\alpha = 0$, evaluating the phase of the spectrum at its maximum yields the correct phase, φ_0, of the signal. In Fig. 6 it is clearly visible that this is not true for signals with a residual chirp, $\alpha \neq 0$. Evaluating the phase of the FFT-based spectra of (16) at its maximum shows that and additional phase error $\Delta\varphi(\alpha)$ is introduced in comparison to a pure sinusoidal. Furthermore, can be concluded from Fig. 6 that the introduced a phase error $\Delta\varphi(\alpha)$, depends linearly on the chirp bandwidth α. In order to quantify the error, a linear regression of $\Delta\varphi(\alpha)$ was carried out and is also shown in Fig. 6. The linear regression results in the following approximation of the phase shift, depending on the chirp bandwidth α.

$$\Delta\varphi(\alpha) \approx -0.333\pi\alpha \tag{19}$$

The spectrum of (16) for chirp bandwidths of $|\alpha| < 0.1$ is therefore approximated by

$$\begin{aligned} X(f) &= \sum_{n=0}^{N-1} A \cdot \mathrm{e}^{\mathrm{j}2\pi \frac{f_0}{f_\mathrm{s}} n} \mathrm{e}^{\mathrm{j}\pi \frac{S}{f_\mathrm{s}^2} n^2} \mathrm{e}^{-\mathrm{j}2\pi \frac{f}{f_\mathrm{s}} n} \\ &\approx A \mathrm{e}^{\mathrm{j}\Delta\varphi(\alpha)} H_N\left(f - (f_0 + \alpha\Delta f)\right). \end{aligned} \tag{20}$$

V. SIGNAL MODEL

The signal model is derived for single Vx channels of a network consisting of 2 sensors with uncoupled oscillators, $\Delta f_{n,m} \neq 0$ Hz. The individual Vx channels are representative of all channels of the 4 sub-apertures. The derived coupling-induced errors for the 4 Vx channels effect all Vx channels on the same sub-aperture equally. For a general network composed of V sensors, the formulas must be evaluated for all $\frac{V^2-V}{2}$ pairs of oscillators, and the derived conditions must be met by all pairs.

For the sake of simplicity, path loss and noise are neglected during the derivation of the signal model to focus on the phases and frequencies. The conditions regarding the reference oscillators are chosen such that there is no loss of resolution in range, velocity, or angular resolution. The conditions are general and applicable to every CS-FMCW radar sensor network. For better understanding, numerical results for the waveform parameters used in the 2-sensor setup are given. The used waveform parameters are listed in Table 2.

A. SINGLE CHIRP MODEL

All sensors are triggered at the mutual frame trigger time t_0, but each sensor introduces a frame trigger jitter t_j. The frame trigger jitter is the time duration between the actual trigger time t_0 and the point in time at which the synthesizer of the sensor actually starts creating the first chirp of the frame. The phase of the first chirp of a frame created by the m-th and n-th sensor is described by

$$\begin{aligned} \varphi_{0,m}(t) &= \int_{t_0}^{t} f_{0,m} + S_m \epsilon \, \mathrm{d}\epsilon \\ &= f_{0,m} t + \frac{S_m}{2} t^2 - f_{0,m} t_0 - \frac{S_m}{2} t_0^2, \end{aligned} \tag{21}$$

TABLE 2. 2-Sensor Radar Network Waveform Parameters

Parameter	Value
Start Frequency f_0	76.124 GHz
End Frequency f_1	77.432 GHz
Slope S	30 MHz µs^{-1}
Effective Bandwidth BW_E	1.2 GHz
Ramp Time T_Up	43.61 µs
ADC Start Time T_S	2 µs
Sampling Time T_ADC	40 µs
Complete Chirp Duration T_R	49.44 µs
Sampling Rate f_s (real)	10 MHz
Number of Tx Channels N_Tx	24
Number of Rx Channels N_Rx	32
Number of Chirps per Vx Channel K	128
Total Measurement Time T_F	152 ms

$$\varphi_{0,n}(t) = f_{0,n} t + \frac{S_n}{2} t^2 - f_{0,n} t_0 - \frac{S_n}{2} t_0^2. \tag{22}$$

The signal after the mixer at the m-th sensor for a static target in the monostatic case is described by

$$\begin{aligned} x_{\mathrm{IF},m,m}(t) &= \mathrm{e}^{\mathrm{j}2\pi\varphi_{0,m}(t-t_{\mathrm{j},m})} \cdot \mathrm{e}^{-\mathrm{j}2\pi\varphi_{0,m}(t-t_{\mathrm{j},m}-\tau)} \\ &= \mathrm{e}^{j2\pi\Delta\varphi_{0,m,m}(t)}. \end{aligned} \tag{23}$$

The phase difference $\Delta\varphi_{0,m,m}(t)$ for a monostatic channel is calculated as

$$\begin{aligned} \Delta\varphi_{0,m,m}(t) &= f_{0,m}(t - t_{\mathrm{j},m}) + \frac{S_m}{2}(t - t_{\mathrm{j},m})^2 \\ &\quad - f_{0,m} t_0 - \frac{S_m}{2} t_0^2 \\ &\quad - f_{0,m}(t - t_{\mathrm{j},m} - \tau) - \frac{S_m}{2}(t - t_{\mathrm{j},m} - \tau)^2 \\ &\quad + f_{0,m} t_0 + \frac{S_m}{2} t_0^2 \\ &= f_{0,m}\tau + S_m \tau t - \cancel{\frac{S_m}{2}\tau^2} - \cancel{S_m \tau t_{\mathrm{j},m}} \\ &\approx \underbrace{f_{0,m}\tau}_{\varphi_\tau} + \underbrace{S_m \tau}_{f_\tau} t. \end{aligned} \tag{24}$$

For automotive radar systems, the term depending on the square of the time-of-flight τ^2 and the term depending on the product of the time-of-flight and the frame trigger jitter, $\tau t_{\mathrm{j},m}$, can be neglected, since they are small in comparison to the phase term linearly depending on the time-of-flight φ_τ. The same calculation carried out for a monostatic channel of the n-th sensor, already neglecting the term depending on τ^2, yields

$$\Delta\varphi_{0,n,n}(t) \approx f_{0,n}\tau + S_n \tau t. \tag{25}$$

The phase difference of monostatic channels consists of a constant phase term φ_τ, which only depends on the time-of-flight τ and is independent of the frame trigger t_0 and the frame trigger jitter t_j. Furthermore, neither the frame trigger nor the

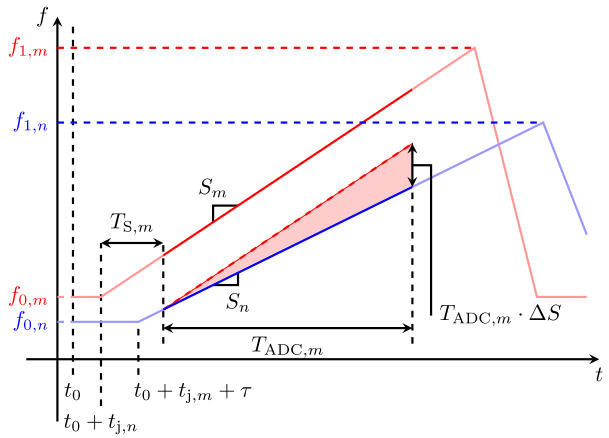

FIGURE 7. Frequency progressions for a bistatic channel.

frame trigger jitter have an influence on the beat frequency f_τ, as described by the phase term depending linearly on time t.

For the bistatic channels it must be taken into account that the start frequency f_0, the slope S, and the frame trigger jitter t_j, are sensor specific. The bistatic frequency progressions are visualized in Fig. 7. Carrying out the calculation of (23) for a bistatic channel and neglecting all parts which depend on t_0^2, yields

$$\begin{aligned}\Delta\varphi_{0,n,m}(t) &= \varphi_{0,n}(t - t_{\mathrm{j},n}) - \varphi_{0,m}(t - t_{\mathrm{j},m} - \tau)\\ &= f_{0,n}(t - t_{\mathrm{j},n}) - f_{0,m}(t - t_{\mathrm{j},m} - \tau)\\ &\quad + \frac{S_n}{2}(t - t_{\mathrm{j},n})^2 - \frac{S_m}{2}(t - t_{\mathrm{j},m} - \tau)^2\\ &\quad - f_{0,n}t_0 + f_{0,m}t_0. \end{aligned} \tag{26}$$

Exploiting the fact that the reference frequencies can be expressed as each other by (2), consequently, the start frequency and the slope can also be expressed as

$$f_{0,n} = f_{0,m} + \Delta f_{0,m,n} \tag{27}$$

$$S_n = S_m + \Delta S_{m,n}. \tag{28}$$

Using (27) and (28) in (26) and resorting the terms yields

$$\begin{aligned}&\Delta\varphi_{0,n,m}(t)\\ &= \left(f_{0,m} + \Delta f_{0,m,n}\right)\left(t - t_{\mathrm{j},n}\right) - f_{0,m}\left(t - t_{\mathrm{j},m} - \tau\right)\\ &\quad + \frac{S_m + \Delta S_{m,n}}{2}(t - t_{\mathrm{j},n})^2 - \frac{S_m}{2}(t - t_{\mathrm{j},m} - \tau)^2\\ &\quad - \left(f_{0,m} + \Delta f_{0,m,n}\right)t_0 + f_{0,m}t_0\\ &= f_{0,m}\left(t_{\mathrm{j},m} - t_{\mathrm{j},n} + \tau\right) - \Delta f_{0,m,n}t_0\\ &\quad - \frac{S_m}{2}\left(t_{\mathrm{j},n}^2 - \left(t_{\mathrm{j},m} + \tau\right)^2\right) + \frac{\Delta S_{m,n}}{2}t_{\mathrm{j},n}^2 - \Delta S_{m,n}t_{\mathrm{j},n}t\\ &\quad + S_m\tau t + S_m\left(t_{\mathrm{j},n} - t_{\mathrm{j},m}\right)t + \Delta f_{0,m,n}t + \frac{\Delta S_{m,n}}{2}t^2. \end{aligned} \tag{29}$$

Since all terms depending on $(t_{\mathrm{j},n}^2 - (t_{\mathrm{j},m} + \tau)^2)$ or $t_{\mathrm{j},n}^2$ are insignificant in comparison to the phase terms linearly dependent on them, (29) is approximated by

$$\begin{aligned}\Delta\varphi_{0,n,m}(t) \approx{}& \overbrace{\underbrace{f_{0,m}\tau}_{\varphi_\tau} + \underbrace{f_{0,m}(t_{\mathrm{j},m} - t_{\mathrm{j},n})}_{\Delta\varphi_{t_\mathrm{j}}} - \underbrace{\Delta f_{0,m,n}t_0}_{\Delta\varphi_{f_\mathrm{c}}}}^{\varphi_{n,m}}\\ &+ \overbrace{\underbrace{(S_m\tau}_{f_\tau} + \underbrace{S_m(t_{\mathrm{j},m} - t_{\mathrm{j},n})}_{\Delta f_{t_\mathrm{j}}} + \underbrace{\Delta f_{0,m,n})}_{\Delta f_{f_\mathrm{c}}}t}^{f_{\mathrm{b},n,m}} - \Delta S_{m,n}t_{\mathrm{j},n}t\\ &+ \frac{\Delta S_{m,n}}{2}t^2. \end{aligned} \tag{30}$$

Comparing (29) with the monostatic signals (24) and (25) shows that additional constant phase terms, additional frequency shifts and a residual chirp are present.

Both the phase and frequency shifts are composed of two error sources; The first error source is the relative frame trigger jitter, $\Delta t_\mathrm{j} = (t_{\mathrm{j},m} - t_{\mathrm{j},n})$, and the second is the frequency difference $\Delta f_{0,m,n}$ caused by the frequency deviation of the reference oscillators. The additional constant phase and additional frequency terms do not influence the range resolution of the network but cause only constant shifts. However, as derived in Section IV-B, the residual chirp $\frac{\Delta S_{m,n}}{2}$ can lead to a loss of resolution if not limited.

Calculating (26) with reversed roles, which means the m-th sensor is now the receiving sensor while the n-th sensor is the transmit sensor, shows that the amount of the additional phase, the additional frequency shifts and the residual chirp are the same, but with opposite sign

$$\begin{aligned}&\Delta\varphi_{0,m,n}(t) = \varphi_{0,m}(t - t_{\mathrm{j},m}) - \varphi_{0,n}(t - t_{\mathrm{j},n} - \tau)\\ &\approx \overbrace{\underbrace{f_{0,m}\tau}_{\varphi_\tau} + \underbrace{f_{0,m}(t_{\mathrm{j},n} - t_{\mathrm{j},m})}_{-\Delta\varphi_{t_\mathrm{j}}} + \underbrace{\Delta f_{0,m,n}t_0}_{-\Delta\varphi_{f_\mathrm{c}}}}^{\varphi_{m,n}}\\ &\quad + \overbrace{\underbrace{(S_m\tau}_{f_\tau} + \underbrace{S_m(t_{\mathrm{j},n} - t_{\mathrm{j},m})}_{-\Delta f_{t_\mathrm{j}}} - \underbrace{\Delta f_{0,m,n})}_{-\Delta f_{f_\mathrm{c}}}t}^{f_{b,m,n}} + \Delta S_{m,n}t_{\mathrm{j},m}t\\ &\quad - \frac{\Delta S_{m,n}}{2}t^2. \end{aligned} \tag{31}$$

Comparing (31) with (29) shows that the influence of the errors are symmetric around the fast time frequency f_τ and the constant phase φ_τ caused by the time-of-flight τ.

1) CONDITION 1

In order to preserve the range resolution for the bistatic channels, the bandwidth covered by the residual chirp during the sampling interval must be lower than a tenth of the frequency resolution. The condition is derived from the analysis in

Section IV-B and is mathematically written as,

$$T_{\mathrm{ADC},m}|\Delta S_{m,n}| \leq \frac{\delta f_{\mathrm{R},m}}{10}. \tag{32}$$

The chirp difference $\Delta S_{m,n}$ is expressed in terms of the reference frequency as

$$\Delta S_{m,n} = S_m - S_n = \frac{\Delta N f_{\mathrm{c},m}}{T_{\mathrm{Up},m}} - \frac{\Delta N(f_{\mathrm{c},m} + \Delta f_{m,n})}{T_{\mathrm{Up},m} + \Delta T_{\mathrm{Up},m,n}}, \tag{33}$$

where ΔN is the difference in the frequency multiplication factor of the fundamental frequency between the start of the chirp and the end of the chirp, as defined in (9). If the timing error $\Delta T_{\mathrm{Up},m,n}$ in an interval of T_{Up} is smaller than $\frac{1}{1000}$, the different T_{Up} durations of the sensors can be neglected $T_{\mathrm{Up},m} \approx T_{\mathrm{Up},n} = T_{\mathrm{Up}}$. This condition is met when

$$\begin{aligned} |\Delta T_{\mathrm{Up},m,n}| &\leq \frac{T_{\mathrm{Up}}}{1000} \\ T_{\mathrm{Up}} \cdot \left(\frac{1}{1 + \frac{|\Delta f_{n,m}|}{f_{\mathrm{c}}}} - 1 \right) &\leq \frac{T_{\mathrm{Up}}}{1000} \\ |\Delta f_{n,m}| &\leq f_{\mathrm{c}} \cdot \left(1 - \frac{1}{1 + \frac{1}{1000}} \right), \end{aligned} \tag{34}$$

is fulfilled. If condition (34) is met, the timing difference during an interval of T_{Up} can be neglected, which also means that the timing interval error during T_{ADC} is neglectable since $T_{\mathrm{ADC}} \leq T_{\mathrm{Up}}$. (32) is then rewritten as

$$\begin{aligned} T_{\mathrm{ADC}} \cdot \left(\frac{|\Delta N f_{\mathrm{c},m} - \Delta N(f_{\mathrm{c},m} + \Delta f_{m,n})|}{T_{\mathrm{Up}}} \right) &\leq \frac{\delta f_{\mathrm{R}}}{10} \\ |\Delta f_{m,n}| &\leq \frac{T_{\mathrm{Up}}}{10 \cdot T_{\mathrm{ADC}}^2 \cdot \Delta N}, \end{aligned} \tag{35}$$

where the second line is the result of algebraic manipulation of the the first line. For the waveform parameters listed in Table 2, (34) requires that the frequency difference of the reference oscillators must fulfill $|\Delta f_{n,m}| \leq 39.96$ kHz. (35) requires that the reference oscillators must have a smaller frequency deviation than $|\Delta f_{n,m}| \leq 83.35$ Hz.

If the conditions are fulfilled, the sampling frequencies of the sensors can be assumed to be equal, $f_{\mathrm{s},m} = f_{\mathrm{s},n} \approx f_{\mathrm{s}}$. This is due to the fact that the nominal sampling frequency is in the MHz region, a sampling frequency difference in the 100 Hz region is therefore neglectable. Moreover, it can be assumed that the fast time frequencies of the monostatic sub-apertures are the same, since the slopes of the sensors are only marginally off and neglectable, $S_n = S_m \approx S$. This also means that the linear frequency shifts caused by the slope difference and the frame trigger jitter, $\Delta S_{m,n} t_{\mathrm{j},m} t$ and $\Delta S_{m,n} t_{\mathrm{j},n} t$, are insignificant and neglectable. But the slope difference $\Delta S_{m,n}$ for the bistatic channels over the course of the entire sampling interval must still be accounted for, since the error accumulates over the duration of the sampling window.

The fast time spectra of the monostatic channels after digitizing and windowing are then described by (14)

$$X_0(f_{\mathrm{R}}) = A\mathrm{e}^{\mathrm{j}\varphi_\tau} H_N(f_{\mathrm{R}} - f_\tau). \tag{36}$$

Due to the residual chirp term ΔS the spectra will additionally be frequency and phase shifted, since the residual chirp terms are present with opposite signs, such that the symmetry between the bistatic channels are preserved. The fast time spectra of the bistatic channels are described by (20):

$$X_{0,n,m}(f_{\mathrm{R}}) = A\mathrm{e}^{\mathrm{j}(\varphi_{n,m} + \Delta\varphi(\alpha))} H_N\left(f_{\mathrm{R}} - \left(f_{\mathrm{b},n,m} + \alpha\Delta f\right)\right) \tag{37}$$

$$X_{0,m,n}(f) = A\mathrm{e}^{\mathrm{j}(\varphi_{m,n} - \Delta\varphi(\alpha))} H_N\left(f_{\mathrm{R}} - \left(f_{\mathrm{b},n,m} - \alpha\Delta f\right)\right). \tag{38}$$

It is important to note that for LF coupled networks, all terms originating from the frequency differences of the reference oscillators are $\Delta f_{0,m,n} = 0$ Hz, including the residual chirp term $\Delta S_{m,n}$. Nevertheless, the relative frame trigger jitter Δt_j still causes a symmetric frequency and phase shift.

B. MULTI CHIRP MODEL

So far only a single chirp of a frame has been considered. (24) repeats K times and the repetition rate in a TDM radar network for the m-th sensor is $\widetilde{T}_{\mathrm{R},m} = N_{\mathrm{Tx}} T_{\mathrm{R},m}$. The phase difference depending on the chirp number k for a monostatic channel is

$$\begin{aligned} \Delta\varphi_{m,m}(t,k) &= \varphi_{k,m}\left(t - t_{\mathrm{j},m} - k\widetilde{T}_{\mathrm{R},m}\right) \\ &\quad - \varphi_{k,m}\left(t - t_{\mathrm{j},m} - k\widetilde{T}_{\mathrm{R},m} - \tau\right) \\ &= \varphi_{0,m,m}(t). \end{aligned} \tag{39}$$

For the monostatic channels, the chirp start time cancels out, so the spectrum of each chirp of a frame is described by (36), regardless of the chirp number k.

Applying the TDFT on the slow time, with $\widetilde{f}_{\mathrm{f}} = \frac{1}{\widetilde{T}_{\mathrm{R}}}$ as the sampling frequency and f_{v} as the fast time frequency variable, yields

$$\begin{aligned} X(f_{\mathrm{R}}, f_{\mathrm{v}}) &= \sum_{k=0}^{K-1} A\mathrm{e}^{\mathrm{j}\varphi_\tau} H_N(f_{\mathrm{R}} - f_\tau)\mathrm{e}^{-\mathrm{j}2\pi \frac{f_{\mathrm{v}}}{\widetilde{f}_{\mathrm{f}}} k} \\ &= A\mathrm{e}^{\mathrm{j}\varphi_\tau} H_N(f_{\mathrm{R}} - f_\tau) \sum_{k=0}^{K-1} 1 \cdot \mathrm{e}^{-\mathrm{j}2\pi \frac{f_{\mathrm{v}}}{\widetilde{f}_{\mathrm{f}}} k} \\ &= A\mathrm{e}^{\mathrm{j}\varphi_\tau} H_N(f_{\mathrm{R}} - f_\tau) H_K(f_{\mathrm{v}}). \end{aligned} \tag{40}$$

This is different for the bistatic channels: The timing error of the chirp repetition time, $\Delta\widetilde{T}_{\mathrm{R},m,n}$, must be taken into account. The phase difference then yields

$$\begin{aligned} &\Delta\varphi_{n,m}(t,k) \\ &= \varphi_n\left(t - t_{\mathrm{j},n} - k\widetilde{T}_{\mathrm{R},n}\right) - \varphi_m\left(t - t_{\mathrm{j},m} - k\widetilde{T}_{\mathrm{R},m} - \tau\right) \\ &= \varphi_{k,n}(t - t_{\mathrm{j},n}) - \varphi_{k,m}\left(t - t_{\mathrm{j},m} - \left(\tau + k\Delta\widetilde{T}_{\mathrm{R},n,m}\right)\right). \end{aligned} \tag{41}$$

A static target with no velocity appears as a moving target, since the timing difference of the chirp repetition time for the bistatic channels increases over the duration of a frame. Incorporating this in (31)

$$\Delta\varphi_{n,m}(t) = \varphi_n(t - t_{\mathrm{j},n}) - \varphi_m\left(t - t_{\mathrm{j},m} - \left(\tau + k\Delta\widetilde{T}_{\mathrm{R},m,n}\right)\right)$$
$$\approx \overbrace{\varphi_{n,m} + \underbrace{f_{0,m}\Delta\widetilde{T}_{\mathrm{R},m,n}}_{f_{\mathrm{d},n,m}}k}^{\varphi_{n,m}+f_{\mathrm{d},n,m}k} + \overbrace{\left(f_{\mathrm{b},n,m} + S\Delta\widetilde{T}_{\mathrm{R},m,n}k\right)}^{f_{\mathrm{b},n,m}+\hat{f}_{\mathrm{b}}k} t, \quad (42)$$

shows that a static target appears as a moving target for a bistatic channel, where the influence of the residual chirp term was absorbed in the static phase $\varphi_{n,m}$ and static frequency $f_{\mathrm{b},n,m}$ variables, for the sake of simplicity. As for an actual moving target, the fast time frequency and the phase become dependent on the chirp number. The spectrum is calculated to

$$X_{n,m}(f_{\mathrm{R}}, f_{\mathrm{v}}) = \sum_{k=0}^{K-1} A\mathrm{e}^{\mathrm{j}(\varphi_{n,m}+f_{\mathrm{d},n,m}k)} H_N\left(f_{\mathrm{R}} - \left(f_{\mathrm{b},n,m} + \hat{f}_{\mathrm{b}}k\right)\right)\mathrm{e}^{-\mathrm{j}2\pi\frac{f_{\mathrm{v}}}{f_{\mathrm{f}}}k}. \quad (43)$$

(43) gives reason to two conditions: First, the change of the fast time frequency over the course of a frame must be smaller than half of a slow time frequency bin in order not to lose any significant velocity resolution. Second, the induced phase progression due to the frequency difference between the reference oscillators should be within the ambiguous velocity of the network, to correctly estimate the velocity and correct the phase shifts from channel to channel due to the TDM-induced phase shifts [17].

1) CONDITION 2

The total frequency migration of the fast time frequency over the course of a complete frame must be limited to avoid significant loss of velocity resolution. This loss results from the fast time frequency spectrum not being evaluated at its maximum for each consecutive chirp. This effect is unavoidable but is assumed to be neglectable if the frequency migration during a frame is smaller than half of the fast time frequency resolution:

$$\left|S\cdot\Delta\widetilde{T}_{\mathrm{F},m,n}\right| \le \frac{\delta f_{\mathrm{R}}}{2}$$
$$S\cdot\overbrace{\underbrace{K\cdot N_{\mathrm{Tx}}\cdot T_{\mathrm{R}}}_{T_F}\cdot\left(\frac{1}{1+\frac{|\Delta f_{n,m}|}{f_{\mathrm{c}}}}-1\right)}^{\Delta\widetilde{T}_{\mathrm{F},m,n}} \le \frac{1}{2\cdot T_{\mathrm{ADC}}}$$
$$|\Delta f_{n,m}| \le f_{\mathrm{c}}\cdot\left(\frac{1}{1+2\cdot T_{\mathrm{ADC}}\cdot K\cdot N_{\mathrm{Tx}}\cdot S\cdot T_{\mathrm{R}}}\right). \quad (44)$$

For the waveform parameters listed in Table 2, the frequency difference must fulfill $|\Delta f_{m,n}| \le 109.7$ mHz.

The condition stated by (44) is greatly eased if the number of Tx elements N_{Tx} or the number of chirps K is reduced. Keeping either N_{Tx} constant while reducing K, or vice versa, is equivalent to reducing the measurement time of a frame. In the end, (44) either limits the measurement time of a frame for a given bandwidth or imposes an increasingly strict condition on the frequency difference as the measurement time increases. If (44) is fulfilled, the dependency of the fast time frequency on the chirp number is neglectable, $f_{\mathrm{b},n,m} + \hat{f}_{\mathrm{b}}k \approx f_{\mathrm{b},n,m}$.

2) CONDITION 3

The last condition on the reference frequency difference stems from the fact that the slow time frequency-induced phase progression over the course of a frame must be within the ambiguous velocity range of the waveform. This condition is stated as

$$\left|f_0\cdot N_{\mathrm{Tx}}\cdot\Delta\widetilde{T}_{\mathrm{R},m,n}\right| \le \left|\frac{1}{2}\right|$$
$$N_0\cdot f_{\mathrm{c}}\cdot N_{\mathrm{Tx}}\cdot T_{\mathrm{R}}\cdot\left(\frac{1}{1+\frac{|\Delta f_{n,m}|}{f_{\mathrm{c}}}}-1\right) \le \left|\frac{1}{2}\right|$$
$$|\Delta f_{n,m}| \le f_{\mathrm{c}}\cdot\left(\frac{1}{1+2\cdot N_0\cdot f_{\mathrm{c}}\cdot N_{\mathrm{Tx}}\cdot T_{\mathrm{R}}}\right). \quad (45)$$

For the waveform parameters listed in Table 2, the frequency difference must be $|\Delta f_{m,n}| \le 220.4$ mHz.

(45) becomes stricter as the unambiguous velocity decreases. This is especially disadvantageous for large TDM radar networks, since every additional Tx channel reduces the unambiguous velocity range. If the conditions of (44) and (45) are met by the reference oscillators, the start frequencies of the individual sensors can be approximated by the nominal one, $f_{0,m} = f_{0,n} \approx f_0$.

The spectra of the bistatic channels are then:

$$X_{n,m}(f_{\mathrm{R}}, f_{\mathrm{v}}) \approx A\mathrm{e}^{\mathrm{j}\varphi_{n,m}} H_N\left(f_{\mathrm{R}} - f_{\mathrm{b},n,m}\right)\sum_{k=0}^{K-1}\mathrm{e}^{\mathrm{j}2\pi f_{\mathrm{d},n,m}k}\mathrm{e}^{-j2\pi\frac{f_{\mathrm{v}}}{f_{\mathrm{f}}}k}$$
$$= A\mathrm{e}^{\mathrm{j}\varphi_{n,m}} H_N\left(f_{\mathrm{R}} - f_{\mathrm{b},n,m}\right) H_K\left(f_{\mathrm{v}} - f_{\mathrm{d},n,m}\right) \quad (46)$$

$$X_{m,n}(f_{\mathrm{R}}, f_{\mathrm{v}}) \approx A\mathrm{e}^{j\varphi_{m,n}} H_N\left(f_{\mathrm{R}} - f_{\mathrm{b},m,n}\right) H_K\left(f_{\mathrm{v}} + f_{\mathrm{d},m,n}\right). \quad (47)$$

The coupling-induced fast time frequency has the same magnitudes for the bistatic channels, but with opposite signs. Since the LF networks do not suffer from timing errors, the slow time frequency shift is not present for this network topology.

VI. ESTIMATION & CORRECTION

In order to coherently process all data, the additional phase, fast frequency and slow frequency shifts, caused by the frame trigger jitter, and the frequency deviation of the reference oscillators must be estimated and corrected for each frame. The slow frequency shift is not present for LF coupled networks and therefore needs not to be estimated or corrected. The

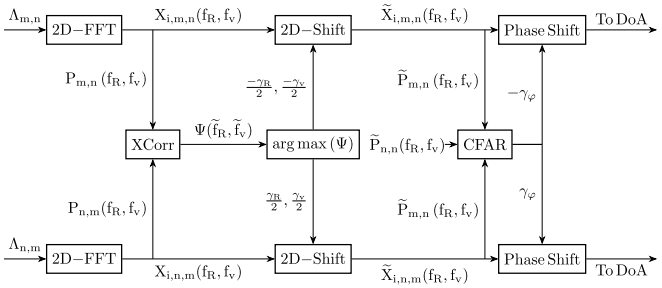

FIGURE 8. Block diagram of the processing chain to estimate and correct the bistatic sub-apertures.

necessary signal processing chain to estimate and correct the data of the bistatic sub-apertures are depicted in Fig. 8.

The derivation of the spectra in Section V was only carried out for single channels of a sub-aperture. But all channels contained on the same bistatic sub-aperture are shifted by the same amount in phase, fast frequency and slow frequency as the single channels.

The estimation of the network coupling-induced shifts in fast frequency, and slow frequency is carried out in the 2D frequency domain,where the coupling-induced errors appear as a simple shift. All power spectra of the channels contained in a set $\Lambda_{m,n}$ are summed to

$$P_{m,n}\left(f_{\mathrm{R}}, f_{\mathrm{v}}\right) = \sum_{i \in \Lambda_{m,n}} \left|X_{i,m,n}\left(f_{\mathrm{R}}, f_{\mathrm{v}}\right)\right|^2. \tag{48}$$

The 2D deterministic cross correlation between two 2D functions is defined as

$$\Psi_{X,Y}\left(\widetilde{f}_{\mathrm{R}}, \widetilde{f}_{\mathrm{v}}\right) = \iint X\left(f_{\mathrm{R}}, f_{\mathrm{v}}\right) Y^*\left(f_{\mathrm{R}} - \widetilde{f}_{\mathrm{R}}, f_{\mathrm{v}} - \widetilde{f}_{\mathrm{v}}\right) \mathrm{d}f_{\mathrm{R}} \mathrm{d}f_{\mathrm{v}}. \tag{49}$$

The shifts of the bistatic channels with respect to the monostatic channels are then estimated by

$$< \gamma_{\mathrm{R}}, \gamma_{\mathrm{v}} >= \arg\max\left(\Psi_{P_{m,n},P_{n,m}}\left(\widetilde{f}_{\mathrm{R}}, \widetilde{f}_{\mathrm{v}}\right)\right). \tag{50}$$

Due to the symmetry between the channels of the two bistatic sub-apertures, both 2D-power spectra are shifted in opposite directions in both domains. The shifts estimated by (50) must be divided by the factor of 2, in order to align the bistatic channels with the monostatic channels and enable coherent processing. This becomes clear if the shift between the two bistatic 2D-power spectra in the fast time frequency domain is calculated as

$$\begin{aligned}\Delta f_{\mathrm{b},(n,m)\to(m,n)} &= f_{\mathrm{b},n,m} - f_{\mathrm{b},m,n} \\ &= \left(f_\tau + \Delta f_{f_{\mathrm{j}}} + \Delta f_{f_{\mathrm{c}}} + \alpha \Delta f\right) \\ &\quad - \left(f_\tau - \Delta f_{f_{\mathrm{j}}} - \Delta f_{f_{\mathrm{c}}} - \alpha \Delta f\right) \\ &= +2\Delta f_{f_{\mathrm{j}}} + 2\Delta f_{f_{\mathrm{c}}} + 2\alpha \Delta f \approx \gamma_{\mathrm{R}}.\end{aligned} \tag{51}$$

The same calculation can be carried out for the phase and the slow time frequency.

The correction can either be carried out in the time domain by multiplying the time signals with a correction signal or in the frequency domain by shifting and resampling all of the 2D-spectra associated with bistatic channels. The time domain method is described by

$$\widetilde{x}_{i,n,m}(t,k) = \mathrm{e}^{-\mathrm{j}2\pi \frac{\gamma_{\mathrm{R}}}{2} t} \mathrm{e}^{-\mathrm{j}2\pi \frac{\gamma_{\mathrm{v}}}{2} k} x_{i,n,m}(t,k), i \in \Lambda_{n,m}, \tag{52}$$

$$\widetilde{x}_{i,m,n}(t,k) = \mathrm{e}^{+\mathrm{j}2\pi \frac{\gamma_{\mathrm{R}}}{2} t} \mathrm{e}^{+\mathrm{j}2\pi \frac{\gamma_{\mathrm{v}}}{2} k} x_{i,m,n}(t,k), i \in \Lambda_{m,n}, \tag{53}$$

where the necessary TDM-induced phase correction terms are omitted.

For LF coupled radar networks, the slow time frequency shift is not present. The 2D-cross correlation can then only be carried out over the fast time frequency $\widetilde{f}_{\mathrm{R}}$ and the correction term for the slow time domain is set to $\gamma_{\mathrm{v}} = 0$.

To coherently estimate the DoA across the whole network, it is necessary to estimate the phase difference between the sub-apertures. This is done with the aid of the redundant Vx antenna elements. After the fast and slow time frequency correction, all channels of the network can be evaluated at a fixed fast and slow time frequency to evaluate the phase terms $\varphi_{m,n}$ and $\varphi_{n,m}$. During the derivation, the fact that the time-of-flight τ is channel specific τ_i was omitted since the time difference between individual channels is neglectable in fast and slow time frequency processing.

Nevertheless, for redundant Vx elements, the time-of-flights are equal, which is exploited to estimate the phase shifts between the sub-apertures $\Lambda_{m,n}$ and $\Lambda_{n,m}$.

A Constant False Alarm Rate (CFAR) algorithm is applied on the corrected 2D-power spectra $P(f_{\mathrm{R}}, f_{\mathrm{v}})$ of the complete network to identify possible targets [18]. The cell with the highest peak prominence is used to estimate the phase difference between the sub-apertures. The phase difference is estimated by calculating the phase difference of all redundant channel pairs in the set $\tilde{\Lambda}_{m,n\to n,m}$, summing over all phase differences and dividing it by the factor of 2. This procedure is described by

$$\gamma_\varphi = \frac{\arg\left(\sum_{i,j} \widetilde{X}_{i,n,m} \widetilde{X}^*_{j,n,m}\right)}{2}, \quad i, j \in \tilde{\Lambda}_{m,n\to n,m}, \tag{54}$$

where $\widetilde{X}_{i,n,m}$ is the 2D-spectrum of the i-th channel evaluated at the cell with the highest peak prominence, $\widetilde{X}_{i,n,m} = X_{i,n,m}(\widetilde{f}_{\mathrm{R,max}}, \widetilde{f}_{\mathrm{v,max}})$. Because the phase difference between the two bistatic sub-apertures can be larger than $|2\pi|$, the estimate γ_φ is ambiguous by $\pm\pi$. To resolve this ambiguity, the sets of redundant Vx channels between the monostatic and the bistatic sub-apertures must be used in addition. The phase difference between a monostatic and bistatic sub-aperture is calculated by

$$\gamma_{\varphi,m} = \arg\left(\sum_{i,j} \widetilde{X}_{i,n,n} \widetilde{X}^*_{j,m,n}\right), \quad i, j \in \tilde{\Lambda}_{n,n\to m,n}. \tag{55}$$

If the magnitude of the difference between (54) and (55) is larger than $|\frac{\pi}{2}|$, the estimate γ_φ must be corrected by $\pm\pi$.

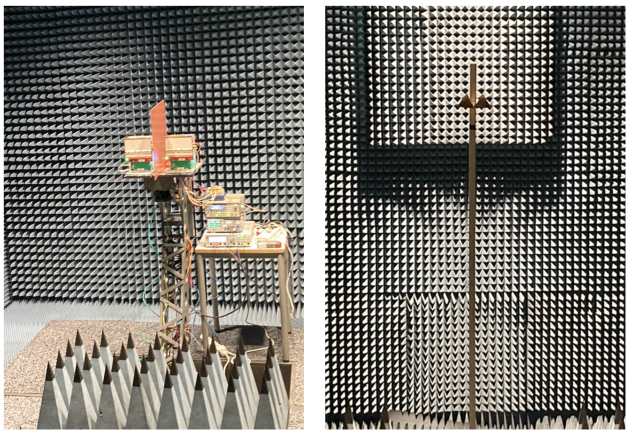

FIGURE 9. Left: 2-Sensor radar network. Right: Measurement target.

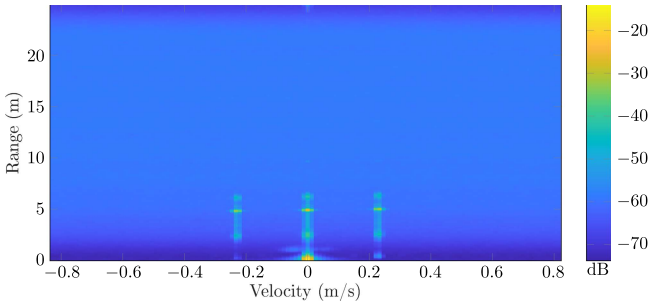

FIGURE 10. 2-Sensor uncoupled network: Uncorrected 2D-power spectrum of the complete network in dB.

This procedure is also applied to the redundant elements of the set $\tilde{\Lambda}_{m,m\to n,m}$ to reduce the probability of a wrong decision regarding the additional addend of $\pm\pi$.

VII. MEASUREMENTS

To verify the signal model and the efficiency of the estimation and correction of the coupling-induced errors, a target consisting of 2 corner reflectors is placed 5 m in front of the radar network. The 2 corner reflectors, with a side length of 6cm are spaced 6cm apart from each other. This means that only the complete network aperture is able to separate the targets in the angular domain. The measurement setup is depicted in Fig. 9.

The reference oscillators are tuned once before the measurements and are free running from that point on. For the LF coupled network measurements, all sensors are connected to the same reference oscillator.

A. UNCOUPLED NETWORK: 2-SENSOR SETUP

The waveform parameters are listed in Table 2. In Fig. 10, the uncorrected 2D-power spectrum of the complete network for a single measurement is depicted. As the theory states, it is clearly visible that the static target around 5 m is split into multiple targets, symmetrically shifted around the correct velocity and range. In order to verify that the symmetrically shifted power spectra originate from the

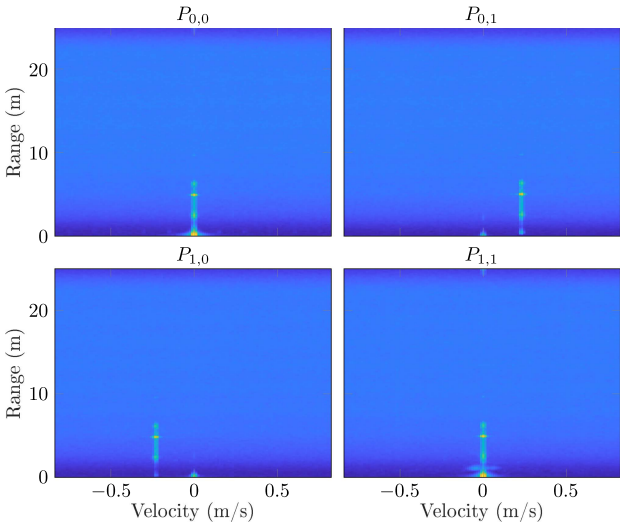

FIGURE 11. 2-sensor uncoupled network: Uncorrected 2D-power spectra of the sub-apertures in dB.

bistatic sub-apertures, the complete network power spectrum $P(f_\mathrm{R}, f_\mathrm{v})$ consisting of 768 Vx channels is split into its sub-aperture power spectra $P_{m,n}(f_\mathrm{R}, f_\mathrm{v})$ of which each one consists of 192 Vx channels. The sub-aperture power spectra, with the same color scaling as in Fig. 10, are depicted in Fig. 11. During the derivation of the signal model, the frame trigger jitter and the frequency deviation between the reference oscillators were treated as constants. To demonstrate the fact that they are frame-to-frame random variables, 90 consecutive frames are evaluated and analyzed. For each frame, the arguments of the maximums of the bistatic 2D-power spectra are evaluated, estimating the target's fast time frequency $f_{\mathrm{b},0,1}$ as well as its slow time frequency $f_{\mathrm{d},0,1}$:

$$< \widetilde{f}_{\mathrm{b},0,1}, \widetilde{f}_{\mathrm{d},0,1} >= \arg\max\left(P_{0,1}\left(f_\mathrm{R}, f_\mathrm{v}\right)\right). \tag{56}$$

$\widetilde{f}_{\mathrm{b},0,1}, \widetilde{f}_{\mathrm{d},0,1}$ are the estimated target frequencies of the bistatic sub-aperture $\Lambda_{0,1}$. This is also carried out for the sub-aperture $\Lambda_{1,0}$. Furthermore, the phase of a redundant Vx channel for each sub-aperture at the estimated frequencies of the target is evaluated,

$$\widetilde{\varphi}_{0,1} = \arg\left(X_{i,0,1}\left(\widetilde{f}_{\mathrm{b},0,1}, \widetilde{f}_{\mathrm{d},0,1}\right)\right) \quad i \in \tilde{\Lambda}_{0,1\to 1,0}, \tag{57}$$

where $\widetilde{\varphi}_{0,1}$ is the estimate of the phase. In Fig. 12 on the left, the time series over 90 frames for the three estimates of the two bistatic sub-apertures $\Lambda_{1,0}$ and $\Lambda_{0,1}$ are displayed. In Fig. 12 on the right, the mean-free scatter plots of the estimates for the two bistatic sub-apertures in addition to their estimated correlation coefficient ρ are shown [19].

The time series representation shows that the influence of the frame timing jitter and the frequency deviation of the reference clocks on the bistatic sub-apertures are symmetric, with the same magnitude but opposite signs. The correlation coefficient in all dimensions exceeds the magnitude of $|\rho| = 0.99$. The mean in f_R is the target-induced fast time frequency f_τ while the mean in f_v represents the residual mean frequency

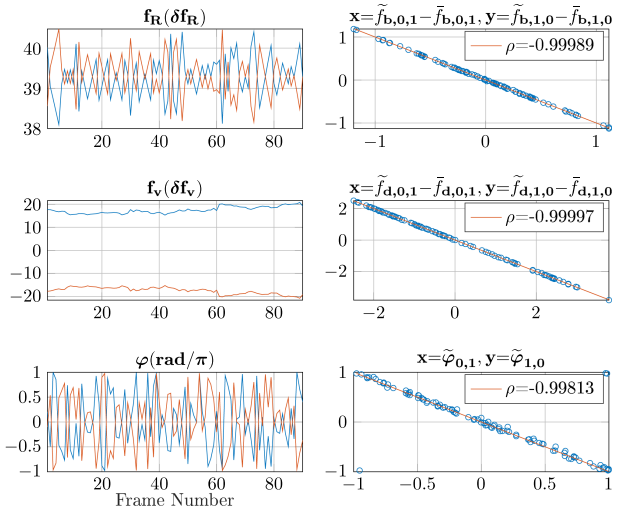

FIGURE 12. 2-Sensor uncoupled network: Correlative analysis of (56) and (57) for $\Lambda_{0,1}$ and $\Lambda_{1,0}$ over 90 consecutive frames. Left: Normalized time series representation: (–)$\Lambda_{1,0}$ and (–)$\Lambda_{0,1}$. Right: Mean-free scatter representation with correlation coefficient.

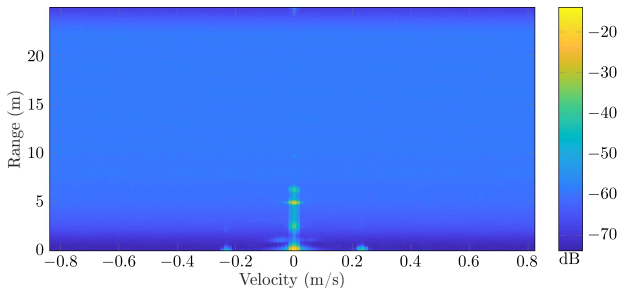

FIGURE 13. 2-Sensor uncoupled network: Corrected 2D-power spectra of the complete network in dB.

difference between the reference oscillators due to imperfect tuning.

The outliers in the scatter representation of the phase are due to uncorrelated noise, which causes a wrap around of $\pm 2\pi$, if the phase errors induced by the frame timing jitter and the frequency difference are in sum close to $|\pi|$. Since this is a representation flaw, the outliers are disregarded in the computation of ρ.

With the basic signal theory proven, the next step is the estimation and correction of the coupling-induced errors. In Fig. 13, the 2D-power spectrum of the complete network is shown after carrying out the estimation and correction described in Section VI. The DoA estimates of the individual sub-apertures, the phase-uncorrected complete network aperture, and the phase corrected complete network aperture are depicted in Fig. 14. The individual sub-apertures are unable to resolve the two corner reflectors, and the uncorrected complete network aperture suffers from high ripple, which makes it impossible to distinguish the side-lobes from the targets. Only with the phase correction, the complete network aperture is able to resolve the two corner reflectors, which means the full resolution is available in the angular domain.

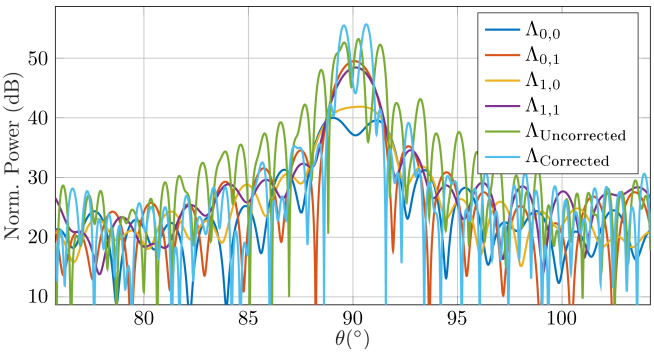

FIGURE 14. 2-Sensor uncoupled network: Azimuth DoA result for all apertures and sub-apertures. Target separation of 0.6°.

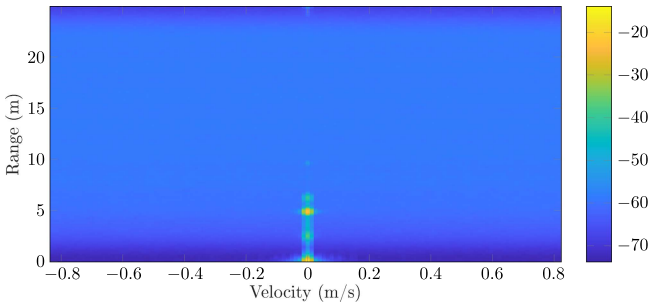

FIGURE 15. 2-Sensor LF coupled network: Uncorrected 2D-power spectra of the complete network in dB.

B. LF COUPLED NETWORK: 2-SENSOR SETUP

The measurements in VII-A were repeated for LF coupling of the network. In Fig. 15, the uncorrected 2Dpower spectra of the complete network is depicted. As expected, no shifts in the velocity dimension are present for the LF coupled network, since the same reference oscillator is provided to the sensors and therefore, no intra frame timing errors exist.

But the frame trigger jitter is present and leads to a symmetric shift in the fast time frequency and a symmetric phase shift for the bistatic sub-apertures. The influence of the frame trigger jitter becomes clearly visible in the correlative analysis. In Fig. 16, the results of the correlative analysis are depicted, where the dimension f_v is omitted since it is not influenced in a LF coupled network.

The distribution in the fast time frequency differs greatly in comparison to the uncoupled network, but the influence remains symmetric. The reason for the different distribution in comparison to the uncoupled network is that there, the influence of the frame trigger jitter and the frequency deviation of the reference clocks overlay. The distribution in an LF network is exclusively caused by the frame trigger jitter. The distribution of the frame trigger jitter is device specific and depends on the implementation of frame triggering by the radar chip manufacturer.

Whether correction of the frame trigger jitter is necessary, solely depends on the distribution of the frame trigger jitter which makes establishing a general condition very difficult. The strictest and most general condition is derived from the

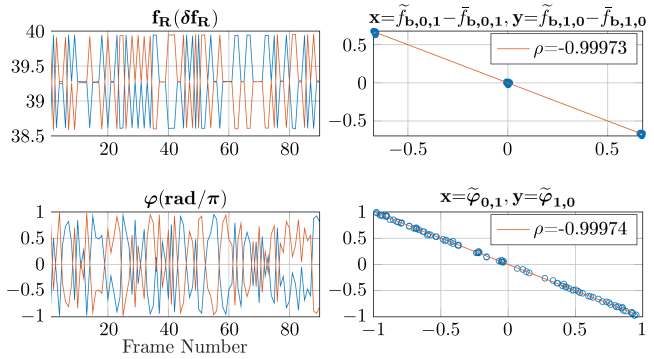

FIGURE 16. 2-Sensor LF coupled network: Correlative analysis of (56) and (57) for $\Lambda_{0,1}$ and $\Lambda_{1,0}$ over 90 consecutive frames.
Left: Normalized time series representation: $(-)\Lambda_{1,0}$ and $(-)\Lambda_{0,1}$.
Right: Mean free scatter representation with correlation coefficient.

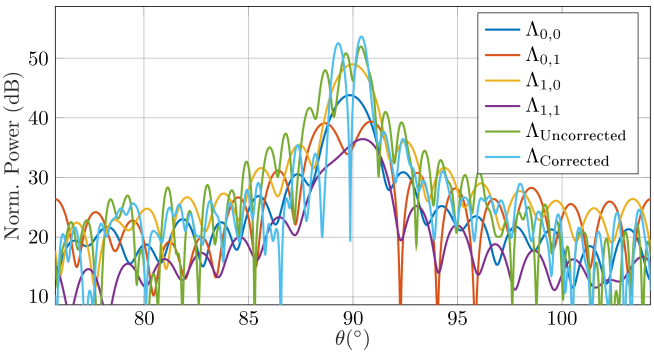

FIGURE 17. 2-Sensor LF coupled network: Azimuth DoA result for all apertures and sub-apertures. Target separation of 0.6°.

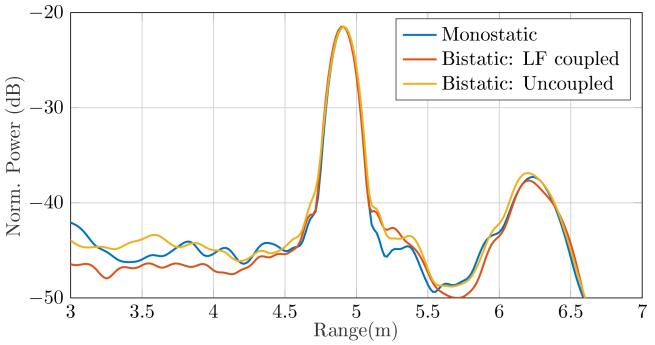

FIGURE 18. Range power spectrum comparison between a monostatic sub-aperture (RF coupled), a LF coupled sub-aperture and an uncoupled sub-aperture.

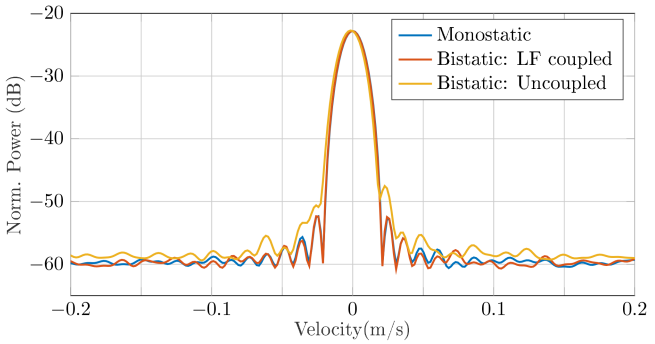

FIGURE 19. Velocity power spectrum comparison between a monostatic sub-aperture (RF coupled), a LF coupled sub-aperture and an uncoupled sub-aperture.

frame trigger jitter induced phase error $\Delta\varphi_{t_j}$. In the case $\Delta\varphi_{t_j} \ll 1$ and therefore neglectable, no correction, neither in the fast time frequency domain nor in the angular domain, is necessary. When this condition is fulfilled, the redundant Vx antenna elements are not required. For the used radar chips, this condition is clearly not fulfilled and correction in the fast time frequency domain and the angular domain are required. The DoA estimates of the individual sub-apertures, the phase-uncorrected complete network aperture, and the phase corrected complete network aperture are depicted in Fig. 17. Just as for the uncoupled network, it is only after the phase correction that the full resolution of the network is available, and the two corner reflectors are separable.

C. COMPARISON BETWEEN RF COUPLED, LF COUPLED AND UNCOUPLED NETWORKS

In order to show that the LF coupled and uncoupled networks do not suffer from any loss in range and velocity resolution in comparison to a RF coupled network, the power spectra of a monostatic sub-aperture is compared to the power spectra of a bistatic sub-aperture for a LF coupled network and an uncoupled network. The monostatic sub-apertures are always RF coupled, since the Rx and Tx signal originate from the same sensor and therefore the same RF synthesizer. The power spectra of the sub-apertures are extracted after the correction. In Fig. 18 the range power spectra, $P(f_R, f_v = 0)$, around the target position are depicted. The sharp peak around 5 m is the target, while the broad peak around 6.2 m is the wall of the anechoic measurement chamber. It can be clearly seen that the target peak has the same width up to around 20 dB below the peak, regardless of whether the sub-aperture is RF coupled, LF coupled or uncoupled. This proves that LF networks and uncoupled networks do not suffer any performance degeneration in terms of range resolution in comparison to RF networks.

In Fig. 19 the velocity power spectra, $P(f_R = f_{R,\mathrm{Target}}, f_v)$, around the target position are depicted. On the one hand, it can be concluded from Fig. 19 that LF networks and uncoupled networks provide the same velocity resolution in comparison to RF coupled networks. On the other hand, it becomes clear that uncoupled radar networks suffer from an increased side lobe level. The reason for this are the timing errors introduced by the fundamental oscillators' frequency deviations. Nevertheless, the side lobe level is only about 5 dB higher than for RF coupled networks and LF coupled networks.

D. UNCOUPLED NETWORK: 3-SENSOR SETUP

To show that the analysis carried out for a single pair of oscillators holds true for all pairs of oscillators in a network

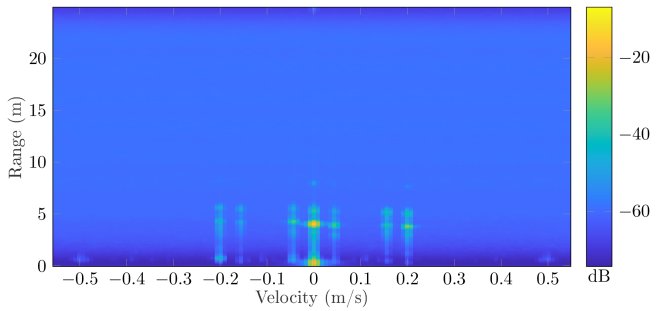

FIGURE 20. 3-Sensor uncoupled network: Uncorrected 2D-power spectra of the complete network in dB.

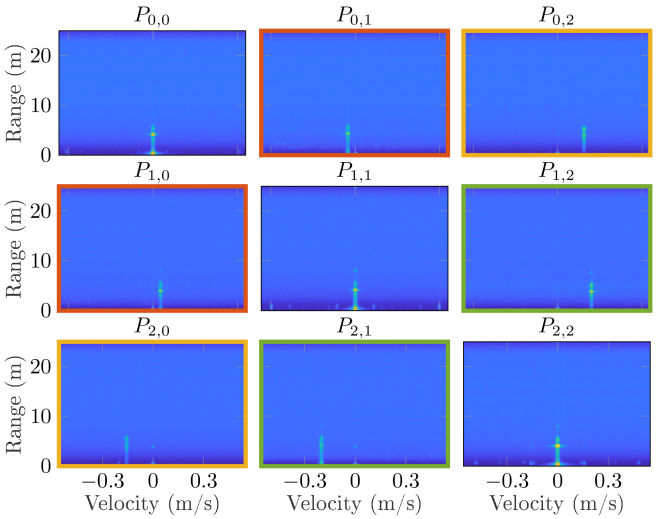

FIGURE 21. 3-Sensor uncoupled network: Uncorrected 2D-power spectra of the sub-apertures in dB.

with more than two sensors, a third identical radar sensor with a randomly distributed antenna array was added to the radar network. The radar network now consists of $V = 3$ radar sensors with $N_{\mathrm{Tx}} = 36$ Tx channels and $N_{\mathrm{Rx}} = 48$ Rx channels, resulting in a total of 1728 Vx channels. Instead of two closely spaced corner reflectors, a single corner reflector was placed at around 4 m in front of the radar network in the anechoic measurement chamber. The intra chirp timing parameters, the number of chirps per Vx channel, and the bandwidth remain the same, which leads to an increase of the total measurement time to $T_{\mathrm{F}} = 228$ ms and a decrease of the unambiguous velocity, due to the extra Tx channels.

The uncorrected 2D-power spectrum of the complete network is depicted in Fig. 20. It is clearly visible that the target is split into 7 targets, shifted in f_{v} and f_{R}. In Fig. 21, the 2D power spectra of each sub-aperture, each consisting of 192 Vx channels, are depicted. With $V = 3$ sensors in the network, 3 pairs of sub-apertures must be taken into account. In Fig. 21, each pair of sub-apertures are highlighted by a colored frame. In order to correct the bistatic sub-apertures and enable coherent processing, the correction steps described

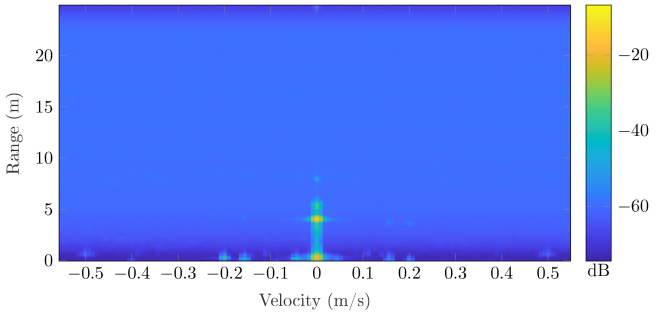

FIGURE 22. 3-Sensor uncoupled network: Corrected 2D-power spectra of the complete network in dB.

TABLE 3. Outdoor Waveform Parameters

Parameter	Value
Start Frequency f_0	76.2 GHz
End Frequency f_1	77.427 GHz
Slope S	52 MHz µs^{-1}
Effective Bandwidth BW_{E}	1 GHz
Ramp Time T_{Up}	23.61 µs
ADC Start Time T_{S}	2 µs
Sampling Time T_{ADC}	20 µs
Complete Chirp Duration T_{R}	27.44 µs
Sampling Rate f_{s} (complex)	10 MHz
Number of Tx Channels N_{Tx}	24
Number of Rx Channels N_{Rx}	32
Number of Chirps per Vx Channel K	32
Total Measurement Time T_{F}	21.1 ms

in Section VI must be carried out for each pair individually. The corrected 2D-power spectrum of the complete network is depicted in Fig. 22.

E. UNCOUPLED NETWORK: 2-SENSOR SETUP OUTDOOR

To prove that the network is able to operate in the absence of a strong single scatter target, an outdoor measurement with a car driving towards the radar network was conducted. The measurement setup is depicted in Fig. 23. The waveform parameters were changed such that a higher unambiguous velocity range and a shorter measurement time are realized in order to keep the range migration effect to a minimum. An added benefit of the greatly reduced chirp repetition time T_{R}, which in combination with the reduced number of chirps per Vx channel K leads to a reduced total measurement time T_{F}, is that the requirements on the frequency difference of the reference oscillators $|\Delta f_{n,m}|$ are eased.

The waveform parameters for the outdoor measurements are listed in Table 3. With the new waveform, (44) requires $|\Delta f_{n,m}| \leq 912.5$ mHz, and (45) requires $|\Delta f_{n,m}| \leq 398.5$ mHz.

In Fig. 23, the uncorrected and corrected 2D-power spectrum of the complete network as well as the spatial 2D-representation of all moving targets are depicted. The power spectra of the bistatic sub-apertures are shifted in f_{R} and f_{v}, but the proposed correction method is able to estimate and

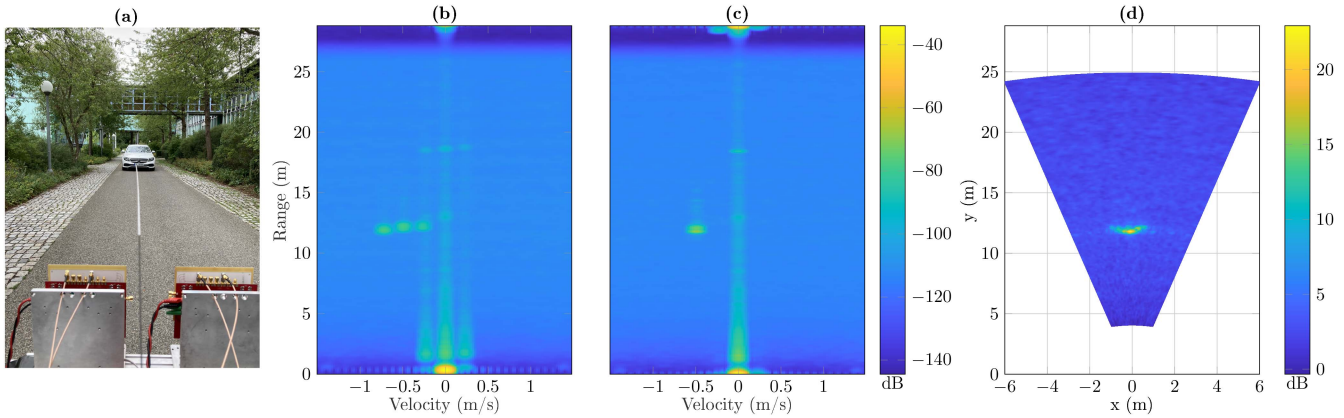

FIGURE 23. 2-Sensors uncoupled network outdoor measurement. (a) Measurement setup and target. (b) Uncorrected 2-power spectrum of the complete network in dB. (c) Corrected 2D-power spectrum of the complete network in dB. (d) x-y-plot in dB.

correct the shifts even for a moving extended target. The phase shifts between the sub-apertures are estimated and corrected, and the front of the car is clearly visible in the spatial representation.

VIII. CONCLUSION

In this paper, a signal model for MIMO radar networks of different topologies has been derived. The model makes it possible to systematically derive conditions regarding the frequency deviation which the reference oscillators must fulfill in order to estimate and correct the coupling-induced errors and enable coherent processing of all radar data in the range, the velocity, and the angular domain. The conditions are universally applicable to all uncoupled radar networks, regardless of the frequency of the reference oscillators, the RF frequency at which the radar operates, or the waveform parameters, since all of those parameters have been accounted for.

For LF coupled radar networks, the conditions in terms of frequency deviation of the reference oscillators are always fulfilled, but the frame trigger jitter induces similar errors in the range and angular domain. The frame trigger jitter distribution is device specific and depends on the implementation of frame triggering by the radar chip manufacturer. The derived model accounts for the frame trigger jitter. Conditions imposed on the frame trigger jitter, which allow for the omission of the estimation and correction of the induced errors, have been discussed.

A radar network consisting of up to 3 radar sensors has been realized, and the measurements proved the signal model for both the uncoupled and LF coupled radar networks. It was shown that the influence of the coupling-induced errors on the radar signal is strictly symmetrical, which allows for simple but yet effective methods of estimation and correction in order to enable coherent radar processing for uncoupled and LF coupled radar networks. The effectiveness of the proposed methods to estimate and correct the coupling-induced errors even for moving extended targets was verified by measurements. Measurements demonstrated that phase noise has insignificant influence on establishing coherency between the sensors.

Even though the derived requirements for the realized radar network, in which the reference oscillator frequency is just 40 MHz and the operating RF frequency is around 77 GHz, are very stringent, it was shown that the requirements can easily be fulfilled by TCVCXO if they are manually tuned. Since the frequency deviation of the reference oscillators is directly measurable by evaluating the 2D-power spectra of sub-apertures, automatic tuning of the reference oscillators is theoretically possible.

REFERENCES

[1] J. Dickmann et al., "Automotive radar the key technology for autonomous driving: From detection and ranging to environmental understanding," in *Proc. IEEE Radar Conf.*, 2016, pp. 1–6.
[2] C. Waldschmidt, J. Hasch, and W. Menzel, "Automotive radar — from first efforts to future systems," *IEEE J. Microwaves*, vol. 1, no. 1, pp. 135–148, Jan. 2021.
[3] D. Werbunat, B. Meinecke, B. Schweizer, J. Hasch, and C. Waldschmidt, "OFDM-based radar network providing phase coherent DOA estimation," *IEEE Trans. Microw. Theory Techn.*, vol. 69, no. 1, pp. 325–336, Jan. 2021.
[4] B. Meinecke, M. Steiner, J. Schlichenmaier, J. Hasch, and C. Waldschmidt, "Coherent multistatic MIMO radar networks based on repeater tags," *IEEE Trans. Microw. Theory Techn.*, vol. 67, no. 9, pp. 3908–3916, Sep. 2019.
[5] M. Gottinger, P. Gulden, and M. Vossiek, "Coherent signal processing for loosely coupled bistatic radar," *IEEE Trans. Aerosp. Electron. Syst.*, vol. 57, no. 3, pp. 1855–1871, Jun. 2021.
[6] A. Frischen, J. Hasch, and C. Waldschmidt, "A cooperative MIMO radar network using highly integrated FMCW radar sensors," *IEEE Trans. Microw. Theory Techn.*, vol. 65, no. 4, pp. 1355–1366, Apr. 2017.
[7] A. Durr, R. Kramer, D. Schwarz, M. Geiger, and C. Waldschmidt, "Calibration-based phase coherence of incoherent and quasi-coherent 160-GHz MIMO radars," *IEEE Trans. Microw. Theory Techn.*, vol. 68, no. 7, pp. 2768–2778, Jul. 2020.
[8] A. Durr, D. Bohm, D. Schwarz, S. Hafner, R. Thoma, and C. Waldschmidt, "Coherent measurements of a multistatic MIMO radar network with phase noise optimized non-coherent signal synthesis," *IEEE J. Microwaves*, vol. 2, no. 2, pp. 239–252, Apr. 2022.
[9] M. Budge and M. Burt, "Range correlation effects in radars," in *Proc. Rec. IEEE Nat. Radar Conf.*, 1993, pp. 212–216.
[10] V. Janoudi et al., "Antenna array design for coherent MIMO radar networks," in *Proc. IEEE Radar Conf.*, 2023, pp. 1–6.

[11] A. Frischen, G. Hakobyan, and C. Waldschmidt, "Coherent measurements with MIMO radar networks of incoherent FMCW sensor nodes," *IEEE Microw. Wireless Compon. Lett.*, vol. 30, no. 7, pp. 721–724, Jul. 2020.
[12] R. E. Best, *Phase-Locked Loops: Design, Simulation, and Applications.* New York, NY, USA: McGraw-Hill, 2006.
[13] D. M. Pozar, *Microwave Engineering.* Hoboken, NJ, USA: Wiley, 2012.
[14] B. Meinecke, D. Werbunat, Q. Haidari, M. Linder, and C. Waldschmidt, "Near-field compensation for coherent radar networks," *IEEE Microw. Wireless Compon. Lett.*, vol. 32, no. 10, pp. 1251–1254, Oct. 2022.
[15] A. Oppenheim and R. Schafer, *Discrete-Time Signal Processing.* Upper Saddle River, NJ, USA: Pearson, 2013.
[16] F. Harris, "On the use of windows for harmonic analysis with the discrete fourier transform," *Proc. IEEE IRE*, vol. 66, no. 1, pp. 51–83, Jan. 1978.
[17] J. Bechter, F. Roos, and C. Waldschmidt, "Compensation of motion-induced phase errors in TDM MIMO radars," *IEEE Microw. Wireless Compon. Lett.*, vol. 27, no. 12, pp. 1164–1166, Dec. 2017.
[18] H. Rohling, "Radar CFAR thresholding in clutter and multiple target situations," *IEEE Trans. Aerosp. Electron. Syst.*, vol. AES-19, no. 4, pp. 608–621, Jul. 1983.
[19] M. Kutner, C. Nachtsheim, and J. Neter, *Applied Linear Statistical Models*, 5th ed. New York, NY, USA: McGraw-Hill, 2004.

VINZENZ JANOUDI (Graduate Student Member, IEEE) received the M.Sc. degree in electrical engineering from the University of Applied Sciences of Karlsruhe, Karlsruhe, Germany, in 2018 and the M.Eng degree from Toronto Metropolitan University, Toronto, ON, Canada, in 2019. He is currently working toward the Ph.D. degree in electrical engineering with the Institute of Microwave Engineering, University Ulm, Ulm, Germany. In 2015 and 2016, he was with Rohde & Schwarz, Munich, Germany, as a Bachelor Thesis Student and Development Engineer. In 2018, he was with Bosch Corporate Research as a Master Thesis Student in the field of distributed source coding. From 2019 to 2020, he was with PLATH Group as a Development Engineer for signal intelligence receivers and direction finders. Since 2020, he has been a Research Assistant with the University Ulm. His research interests include communication systems, system concepts for radar networks, and the accompanying signal processing.

PIRMIN SCHOEDER (Member, IEEE) received the B.Sc. and M.Sc. degrees in electrical engineering from the University of Ulm, Ulm, Germany, in 2017 and 2019, respectively, where he is currently working toward the Ph.D. degree with the Institute of Microwave Engineering. In 2019, he was an Intern with Rohde & Schwarz, Singapore. His research interests include system concepts and signal processing for radar target simulators.

TIMO GREBNER (Graduate Student Member, IEEE) received the master's degree in electrical engineering from Ulm University, Ulm, Germany, in 2019, where he is currently working toward the Ph.D. degree in electrical engineering with the Institute of Microwave Engineering. In 2018, he was an Intern with Sony, Japan. His research focuses on the creation of high-resolution occupancy gridmaps by high accuracy ego-motion estimations in a distributed and collaborative radar sensor topology.

NILS APPENRODT (Senior Member, IEEE) received the Dipl.-Ing. degree in electrical engineering from University Duisburg, Duisburg, Germany, in 1996. He was a Research Assistant in the field of imaging radar systems with University Duisburg. Since 2000, he has been with the Group Research and Advanced Engineering, formerly Daimler AG now Mercedes-Benz AG, as a Research Engineer and Manager, where he is working in the field of environment perception systems. His research interests include radar sensor processing, sensor data fusion, advanced driver assistance, and autonomous driving systems.

JUERGEN DICKMANN (Senior Member, IEEE) received the Diploma degree in electrical engineering from University Duisburg, Duisburg, Germany, in 1984 and the Dr.-Ing. degree from Rheinisch Westfaelische Technische Hochschule Aachen (RWTH), Aachen, Germany. In 1986, he started his career with AEG Research Center, where he did research on III/V-semiconductor processing techniques, mm-wave device, and MMIC-design (up to 120 GHz) and fabrication. He is the Head of radar sensors and radar-based perception at autonomous driving, Mercedes-Benz AG. In this role, he is responsible for research to serial development of radar and radar-based environmental understanding for autonomous driving for all platforms inside Mercedes-Benz AG. Among others, he held manager positions with Daimler AG in laser-scanner, sensor-fusion, and situation analysis. He conducted radar developments for radar-based precrash and driver assistant systems for all platforms (passenger cars, buses, van, truck) inside Daimler AG, including E/S-Class.

CHRISTIAN WALDSCHMIDT (Fellow, IEEE) received the Dipl.-Ing. (M.S.E.E.) and Dr.-Ing. (Ph.D.E.E.) degrees from the University Karlsruhe, Karlsruhe, Germany, in 2001 and 2004, respectively. From 2001 to 2004, he was a Research Assistant with the Institut für Höchstfrequenztechnik and Elektronik, Universität Karlsruhe. Since 2004, he has been with Robert Bosch GmbH, in the business units Corporate Research and Chassis Systems. He was heading different research and development teams in microwave engineering, RF-sensing, and automotive radar. In 2013, he returned to academia. He was appointed as the Director of the Institute of Microwave Engineering, University Ulm, Ulm, Germany, as Full Professor. He has authored or coauthored more than 200 scientific publications and more than 20 patents. His research interests include radar and RF-sensing, mm-wave and submillimeterwave engineering, antennas and antenna arrays, and RF and array signal processing. He is a Member of the Executive Committee Board of the German MTT/AP joint chapter and a Member of the German Information Technology Society. He is the Chair of the IEEE MTT-29 Technical Committee on Microwave Aerospace Systems and was the Chair of MTT-27 Technical Committee on Wireless Enabled Automotive and Vehicular Applications. He was a two-time TPC Chair and General Chair of the IEEE MTT International Conference on Microwaves for Intelligent Mobility. Since 2018, he has been an Associate Editor for IEEE MTT MICROWAVE WIRELESS COMPONENTS LETTERS. He is a reviewer for multiple IEEE transactions and many IEEE conferences in the field of microwaves. He was a co-recipient of 13 best paper awards since 2014.